

Recordings and Analysis of Atomic Ledge and Dislocation Movements in InGaAs to Nickelide Nanowire Phase Transformation

Renjie Chen* and Shadi A. Dayeh*

The formation of low resistance and self-aligned contacts with thermally stable alloyed phases is a prerequisite for realizing reliable functionality in ultrascaled semiconductor transistors. Detailed structural analysis of the phase transformation accompanying contact alloying can facilitate contact engineering as transistor channels approach a few atoms across. Original in situ heating transmission electron microscopy studies are carried out to record and analyze the atomic scale dynamics of contact alloy formation between Ni and $\text{In}_{0.53}\text{Ga}_{0.47}\text{As}$ nanowire channels. It is observed that the nickelide reacts on the $\text{In}_{0.53}\text{Ga}_{0.47}\text{As}$ (111) || $\text{Ni}_2\text{In}_{0.53}\text{Ga}_{0.47}\text{As}$ (0001) interface with atomic ledge propagation along the $\text{Ni}_2\text{In}_{0.53}\text{Ga}_{0.47}\text{As}$ [10 $\bar{1}$ 0] direction. Ledges nucleate as a train of strained single-bilayers and propagate in-plane as double-bilayers that are associated with a misfit dislocation of $\bar{b} = \frac{2c}{3}[0001]$. The atomic structure is reconstructed to explain this phase transformation that involves collective gliding of three Shockley partials in $\text{In}_{0.53}\text{Ga}_{0.47}\text{As}$ lattice to cancel out shear stress and the formation of misfit dislocations to compensate the large lattice mismatch in the newly formed nickelide phase and the $\text{In}_{0.53}\text{Ga}_{0.47}\text{As}$ layers. This work demonstrates the applicability of interfacial disconnection (ledge + dislocation) theory in a nanowire channel during thermally induced phase transformation that is typical in metal/III–V semiconductor reactions.

R. Chen
Department of Electrical and Computer Engineering
University of California San Diego
La Jolla, CA 92093, USA
E-mail: recoo6@ucsd.edu

Prof. S. A. Dayeh
Department of Electrical and Computer Engineering
Materials Science and Engineering Program
Department of NanoEngineering
University of California San Diego
La Jolla, CA 92093, USA
E-mail: sdayeh@ucsd.edu



 The ORCID identification number(s) for the author(s) of this article can be found under <https://doi.org/10.1002/sml.201604117>.

DOI: 10.1002/sml.201604117

1. Introduction

Semiconductor nanowires^[1–4] and Fins^[5–7] are promising building blocks for next generation ultrascaled devices for electronic^[8–10] and optoelectronic^[11–13] applications. An important aspect for the development, maturity, and efficiency of these ultrascaled devices is the detailed understanding of and control over the phase transformation that accompanies the formation of their alloyed contacts for lithography-free self-aligned gate design.^[14–16] Prior pioneering research has revealed the large differences between the nanoscale metallization processes with their bulk counterparts, evoking reevaluation of the thermodynamics,^[17] kinetics,^[18,19] and resultant phases^[20] in alloyed and compound nanoscale contacts.^[21,22] The majority of these studies

were carried out by in situ heating and imaging inside a transmission electron microscopy (TEM)^[23–25] which proved powerful in investigating these thermally driven phase transformations in real-time and at atomic resolutions.^[26–29] For instance, it has been found that the ledge nucleation and movement in nanoscale metallization processes can be largely affected by the involved material systems,^[30] local defects,^[31] metal impurities,^[32] dielectric layer coating,^[33] and interfacial properties in between the metal contact and the semiconductor.^[34] Though prominent discoveries have been made on nanostructures on elemental semiconductors, i.e., Si and Ge nanowires,^[22] detailed ledge behaviors have not been uncovered in III–V nanowire channels at atomic resolutions,^[30] possibly due to the multifold elements and complicated phases involved in the phase transformation from a binary/ternary compound semiconductor to a ternary/quaternary compound metallic contact, respectively, even for a single element metal contact (e.g., Ni).

We focus on the narrow band gap high electron mobility III–V semiconductor, $\text{In}_x\text{Ga}_{1-x}\text{As}$, due to its potential in sub-7 nm metal–insulator–semiconductor field-effect transistors.^[35] Among the different compositions of these ternary phases ($\text{In}_x\text{Ga}_{1-x}\text{As}$), $\text{In}_{0.53}\text{Ga}_{0.47}\text{As}$ is most commonly used, as it can be epitaxially grown on an InP substrate and possesses an intermediate energy band-edge gap that simultaneously affords high electron mobility, low Schottky barrier contacts, and low thermally generated leakage currents.^[36] Ni has been argued as a suitable alloyed metal contact with $\text{In}_{0.53}\text{Ga}_{0.47}\text{As}$ channels because it forms a metallic nickelide phase ($\text{Ni}_x\text{In}_{0.53}\text{Ga}_{0.47}\text{As}$)^[37–39] which is analogous to the nickel silicide (Ni_xSi) to the Si material. For these planar device geometries, it was found that at temperatures as low as ≈ 230 °C, a poly-crystalline nickelide phase forms and can be thermally stable up to 450 °C.^[40] The $\text{Ni}_x\text{In}_{0.53}\text{Ga}_{0.47}\text{As}$ lattice is of the NiAs (B8) structure with commonly observed stoichiometry of $\text{Ni}_2\text{In}_{0.53}\text{Ga}_{0.47}\text{As}$ ^[41,42] or $\text{Ni}_3\text{In}_{0.53}\text{Ga}_{0.47}\text{As}$ ^[43,44] at different process conditions. However, the lattice mismatch between $\text{In}_{0.53}\text{Ga}_{0.47}\text{As}$ and the formed $\text{Ni}_x\text{In}_{0.53}\text{Ga}_{0.47}\text{As}$ could introduce large strain in the $\text{In}_{0.53}\text{Ga}_{0.47}\text{As}$ nanowire channels and leads to the formation of defects at the $\text{In}_{0.53}\text{Ga}_{0.47}\text{As}/\text{Ni}_x\text{In}_{0.53}\text{Ga}_{0.47}\text{As}$ interface,^[45] which further complicates detailed structural analysis. Therefore, we sought a detailed investigation of the nucleation and ledge propagation behaviors to uncover the origin of these complicated phase-transformation details.

2. Results and Discussions

In this work, we utilized the in situ TEM heating technique to observe the solid-state reactions between Ni contact and $\text{In}_{0.53}\text{Ga}_{0.47}\text{As}$ nanowire channels. The horizontal $\text{In}_{0.53}\text{Ga}_{0.47}\text{As}$ nanowire channels were fabricated by top-down dry-etch on a separate substrate (details in methods), with nanowires sitting on a 15 nm HfO_2 layer.^[45,46] As shown in **Figure 1a–i**, the nanowire channels were patterned in columns with wire-to-wire distance of 120 nm within a single column, and between adjacent columns a wire-to-wire offset of 30 nm. This design ensures no overlapping

of nanowire channels in a focused-ion-beam (FIB) milled specimen lamella (**Figure 1a–iii**) along the channel direction, and the existence of 2–3 consecutive nanowire channels in this lamella for in situ studies (Section I, Supporting Information). We used the FEI Tecnai F30 TEM and Aduro 500 heating stage (Protochips Inc.) to perform the in situ heating experiments in this work with its compatible AHA thermal E-chips (Protochips Inc.) that served as the heating platform (shown in **Figure 1a–iv**). On top of the chip, two outer metal leads provided resistive heating through the conductive ceramic membrane underneath and another two inner metal leads served as a thermocouple giving temperature feedback to the controller. Then, we again used the FIB to mill an open square on the ceramic membrane and to deposit two Pt posts on opposite sides of the square window (**Figure 1a–v**). Subsequently, the specimen lamella was lifted out and transferred on top of the membrane of a thermal E-chip horizontally (schematic in **Figure 1a–vi**, SEM image in **Figure 1b**) with an Omniprobe inside an SEM (FEI Nova 600) chamber. Finally, this lamella was further thinned to a thickness of 60–80 nm permitting electron beam transparency (**Figure S2**, Supporting Information). The nanowire channel investigated in our in situ heating experiment is labeled in the TEM image in **Figure 1c**.

Figure 2a provides an overview of the interfacial profile between $\text{In}_{0.53}\text{Ga}_{0.47}\text{As}$ nanowire and the reacted nickelide phase after applying the in situ heating at 320 °C (**Movie S1**, Supporting Information). Debates exist in the literature regarding the stoichiometry of Ni when it forms nickelide compounds with $\text{In}_{0.53}\text{Ga}_{0.47}\text{As}$,^[41,44] and the variability of the results can be attributed to the nonequilibrium conditions of short-time annealing, and the sensitivity of the reaction products to the substrates and process temperatures.^[42] However, as it will be shown later in this work, the ledge mechanisms for phase transformation is unaffected by the Ni stoichiometry due to the same hexagonal lattice structure and similar *c/a* ratios for the different nickelide compounds. Here, we deduced the nickelide phase as $\text{Ni}_2\text{In}_{0.53}\text{Ga}_{0.47}\text{As}$ by cross examining the lattice constant (**Figure 2c**) with known value for this phase (more details in the Experimental Section).^[41] From the diffraction patterns of two phases across the interface (**Figure 2b,c**), we found that the interface followed the $\text{In}_{0.53}\text{Ga}_{0.47}\text{As}$ (111) \parallel $\text{Ni}_2\text{In}_{0.53}\text{Ga}_{0.47}\text{As}$ (0001) atomic planes, in agreement with our earlier ex situ studies.^[45] To better understand the interfacial atomic arrangements, ledge formation and movement behaviors, we recorded the nickelide reaction with high-resolution TEM (HRTEM) at $\times 1$ M magnification (**Movie S2**, Supporting Information) and extracted the time-resolved sequences from the digital video (shown in **Figure 2d**, original TEM images without labels are shown in **Figure S3** of the Supporting Information). To the best of our knowledge, this is the first in situ observation of solid-state reaction between metal and III–V nanowires with atomic resolution and that clearly exhibits the ledge formation and movement behaviors.

We found that the $\text{Ni}_2\text{In}_{0.53}\text{Ga}_{0.47}\text{As}$ ledge formed in a train of single-bilayers,^[47] as observed near the top surface of the nanowire channel in each time frame of **Figure 2d**. These single-bilayer ledges were under biaxial tensile stresses from inside the interfacial plane ($\text{In}_{0.53}\text{Ga}_{0.47}\text{As}$

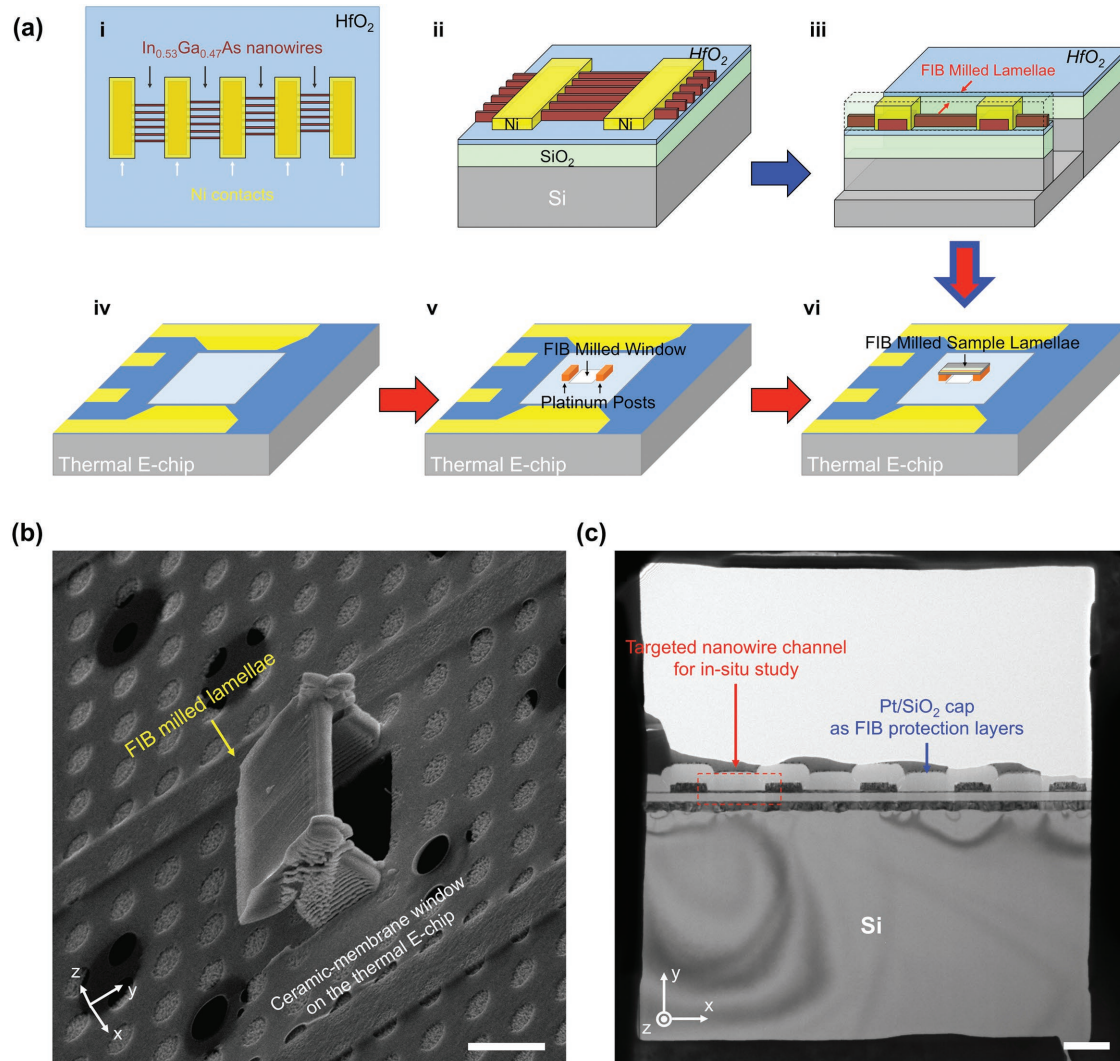


Figure 1. Schematics, SEM, and TEM images that exhibit the FIB mill and lift-out processes for transferring the specimen lamellae onto the TEM membrane window. a) Schematics of the process flow, with i–iii representing the FIB process on device substrate and iv–vi representing the transfer process on TEM thermal E-chips. (i) and (ii) are the top-view and partial side-view of the fabricated $\text{In}_{0.53}\text{Ga}_{0.47}\text{As}$ nanowire channels with Ni contacts. In each column of nanowires, the center-to-center distance is 120 nm, and the channel length is 1 μm . Between two columns, there is an offset of 30 nm. (iii) shows the FIB milling process with the lamellae in parallel with nanowire channel direction. (iv) is the schematic for thermal E-chips. Four metal leads on the thermal E-chip will be connected with the probes on Aduro TEM heating stage to introduce resistive heating and to read out temperatures. (v) shows the FIB milled opening window on the TEM membrane, together with the FIB deposited Pt posts besides. (vi) is the lift-out and transfer step that places the specimen lamellae onto the Pt posts atop the thermal E-chip. c) SEM image of the FIB milled specimen lamellae transferred horizontally onto the TEM membrane on the thermal E-chip. d) TEM image showing the overview of specimen lamellae and the labeled location of nanowire channel for this in situ study.

(111) \parallel $\text{Ni}_2\text{In}_{0.53}\text{Ga}_{0.47}\text{As}$ (0001)) due to lattice mismatch of 5.5%, and a uniaxial compressive stress in the direction that is perpendicular to the interfacial plane due to nickelide volume expansion of 34.2%.^[45] These two effects, in principle, add up the compression of $\text{Ni}_2\text{In}_{0.53}\text{Ga}_{0.47}\text{As}$ lattice in the out-of-plane directions. While in our case here, the very thin (<80 nm) TEM sample lamellae in this study facilitate volume expansion laterally perpendicular to the channel and reduces the overall influence of volume expansion on interfacial stresses. Our observations show that these single-bilayer ledges moved freely along the $[10\bar{1}0]$ direction on the $\text{Ni}_2\text{In}_{0.53}\text{Ga}_{0.47}\text{As}$ (0001) surface from the nanowire top surface to the center region, until hindered by a misfit dislocation that is generated to release the compressive stress during the ledge propagation

(strain analysis is presented in Section IV, Supporting Information). Those newly generated misfit dislocations were captured in the time duration of 0''00''–14''05'' and are marked with a cyan colored arrow, the time duration of 9''49''–14''05'' with a green colored arrow, and the time duration of 32''39''–36''55'' with an orange colored arrow. Once a misfit dislocation is formed, the propagation speed of a single-bilayer ledge decreased and another single-bilayer ledge growth can reach the same $\text{Ni}_2\text{In}_{0.53}\text{Ga}_{0.47}\text{As}/\text{In}_{0.53}\text{Ga}_{0.47}\text{As}$ of the first single bilayer. The ledge with a double-bilayer height moved together thereafter with a misfit dislocation of $\bar{b} = \frac{2c}{3}[0001]$. Even though double-bilayer ledges could instantly merge and then separate into independent double-bilayer ledges in the following movements (e.g., time duration of 0''00''–9''49'',

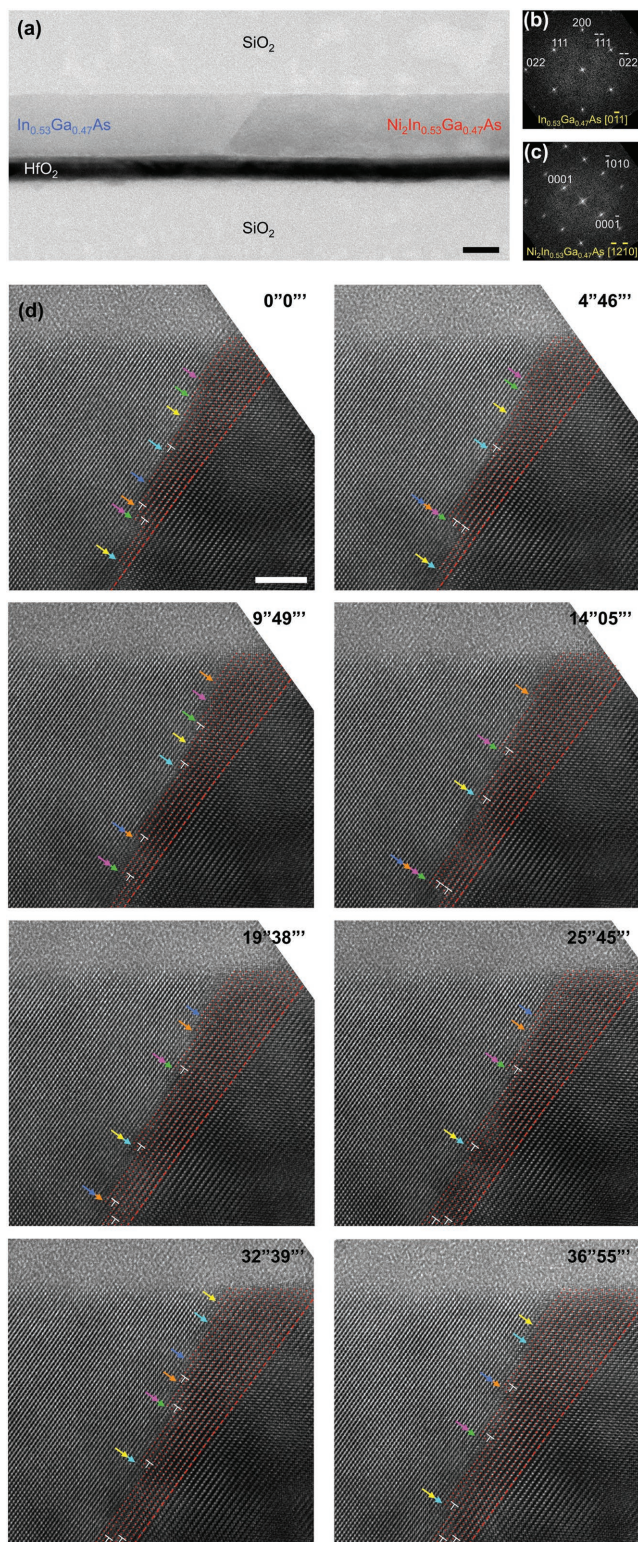


Figure 2. Ledge formation and movement mechanisms of nickelide phase at atomic resolution. a) TEM image of the $\text{In}_{0.53}\text{Ga}_{0.47}\text{As}/\text{Ni}_2\text{In}_{0.53}\text{Ga}_{0.47}\text{As}$ interface showing a slanted interfacial profile. Scale bar is 20 nm. b,c) Fast Fourier transform (FFT) images of the $\text{In}_{0.53}\text{Ga}_{0.47}\text{As}$ and $\text{Ni}_2\text{In}_{0.53}\text{Ga}_{0.47}\text{As}$ segments, respectively, showing the diffraction patterns of $\text{In}_{0.53}\text{Ga}_{0.47}\text{As}$ along the $[01\bar{1}]$ zone axis (projecting direction in TEM) and of $\text{Ni}_2\text{In}_{0.53}\text{Ga}_{0.47}\text{As}$ along the $[\bar{1}2\bar{1}0]$ zone axis. The diffraction patterns indicate that the slanted interface follows the $\text{In}_{0.53}\text{Ga}_{0.47}\text{As}$ (111) || $\text{Ni}_2\text{In}_{0.53}\text{Ga}_{0.47}\text{As}$ (0001) atomic

ledges related to the two labeled dislocations toward the bottom of the images), a double-bilayer ledge remained stable and never splat into two single-bilayers afterward. This indicates that double-bilayer is the unit height for a moving $\text{Ni}_2\text{In}_{0.53}\text{Ga}_{0.47}\text{As}$ ledge after the generation of a misfit dislocation at the reacting $\text{Ni}_2\text{In}_{0.53}\text{Ga}_{0.47}\text{As}/\text{In}_{0.53}\text{Ga}_{0.47}\text{As}$ interface.

These ledge formation and movement behaviors illuminate significant differences with preceding observations made on metal alloying process in elemental semiconductors such as in Si nanowires. When nickel silicide forms in Si nanowire channels, the immediate adjacent phase to pristine Si is NiSi_2 that has a cubic lattice structure and a lattice constant that is very close to that of Si.^[17,22] Therefore, a coherent heteroepitaxial interface was observed in between Si and NiSi_2 , and the NiSi_2 phase grew by forming ledges of single-bilayer height. However, during the phase transformation in $\text{In}_{0.53}\text{Ga}_{0.47}\text{As}/\text{Ni}_2\text{In}_{0.53}\text{Ga}_{0.47}\text{As}$ system, the large lattice mismatch resulted in a misfit dislocation in every two atomic bilayers in $\text{Ni}_2\text{In}_{0.53}\text{Ga}_{0.47}\text{As}$ (corresponding to every three atomic bilayers in $\text{In}_{0.53}\text{Ga}_{0.47}\text{As}$, as will be discussed in detail below). The ledges of $\text{Ni}_2\text{In}_{0.53}\text{Ga}_{0.47}\text{As}$ moved as a double-bilayer height, coupled with the misfit dislocation. An interface that contains both ledge and misfit dislocation is generally referred to as a “disconnection,”^[48–50] and our in situ observations here are the first direct proof of interfacial disconnection in a nanowire channel during thermally induced phase transformation that is typical in metal/III–V semiconductor reactions.

To gain insight into the atomic arrangement at the interfacial disconnection and the motion of the ledges, we developed atomic models to construct the crystal structures at the $\text{In}_{0.53}\text{Ga}_{0.47}\text{As}/\text{Ni}_2\text{In}_{0.53}\text{Ga}_{0.47}\text{As}$ interface. Consider the two magnified HRTEM images of the interfacial disconnections (in the same nanowire but at different reaction times) as shown in **Figure 3a** (original TEM images without labels are shown in **Figure S4** of Supporting Information). At time t_1 in **Figure 3a**, one can observe a clear correlation between three layers of $\text{In}_{0.53}\text{Ga}_{0.47}\text{As}$ lattice planes (marked with yellow dashed lines) and two layers of $\text{Ni}_2\text{In}_{0.53}\text{Ga}_{0.47}\text{As}$ lattice planes (marked with red dashed lines). Therefore, the interface is characterized with a misfit dislocation with a Burgers vector $\vec{b} = \frac{a}{3}[111]$, where $a = 5.87 \text{ \AA}$ is the lattice constant of the $\text{In}_{0.53}\text{Ga}_{0.47}\text{As}$ (zinc-blende). For $\text{Ni}_2\text{In}_{0.53}\text{Ga}_{0.47}\text{As}$ that has a hexagonal lattice with lattice constants of $a = 3.93 \text{ \AA}$ and $c = 5.10 \text{ \AA}$,^[45] (the Burgers vector defined above is equivalent to $\frac{2c}{3}[0001]$). At time t_2 in **Figure 3a**, we observe the same behavior, where a double-bilayer step height is observed. Shown in **Figure 3b** are the lattice structures of zinc-blende $\text{In}_{0.53}\text{Ga}_{0.47}\text{As}$ and hexagonal $\text{Ni}_2\text{In}_{0.53}\text{Ga}_{0.47}\text{As}$. Along the $[111]$ direction of $\text{In}_{0.53}\text{Ga}_{0.47}\text{As}$ crystal, atomic

planes. d) HRTEM sequences extracted from a short time period in **Movie S1** of the Supporting Information, showing the ledge formation at the top-surface of nanowire channel and ledge propagations into the nanowire body. The ledges started with a completely strained single-bilayer form and moved with a double-bilayer step height. This double-bilayer step moved together with a misfit dislocation $\vec{b} = \frac{2c}{3}[0001]$ (labeled by the white “ \perp ”), forming a classic “disconnection” at the interface. All these HRTEM images share the same scale bar of 5 nm.

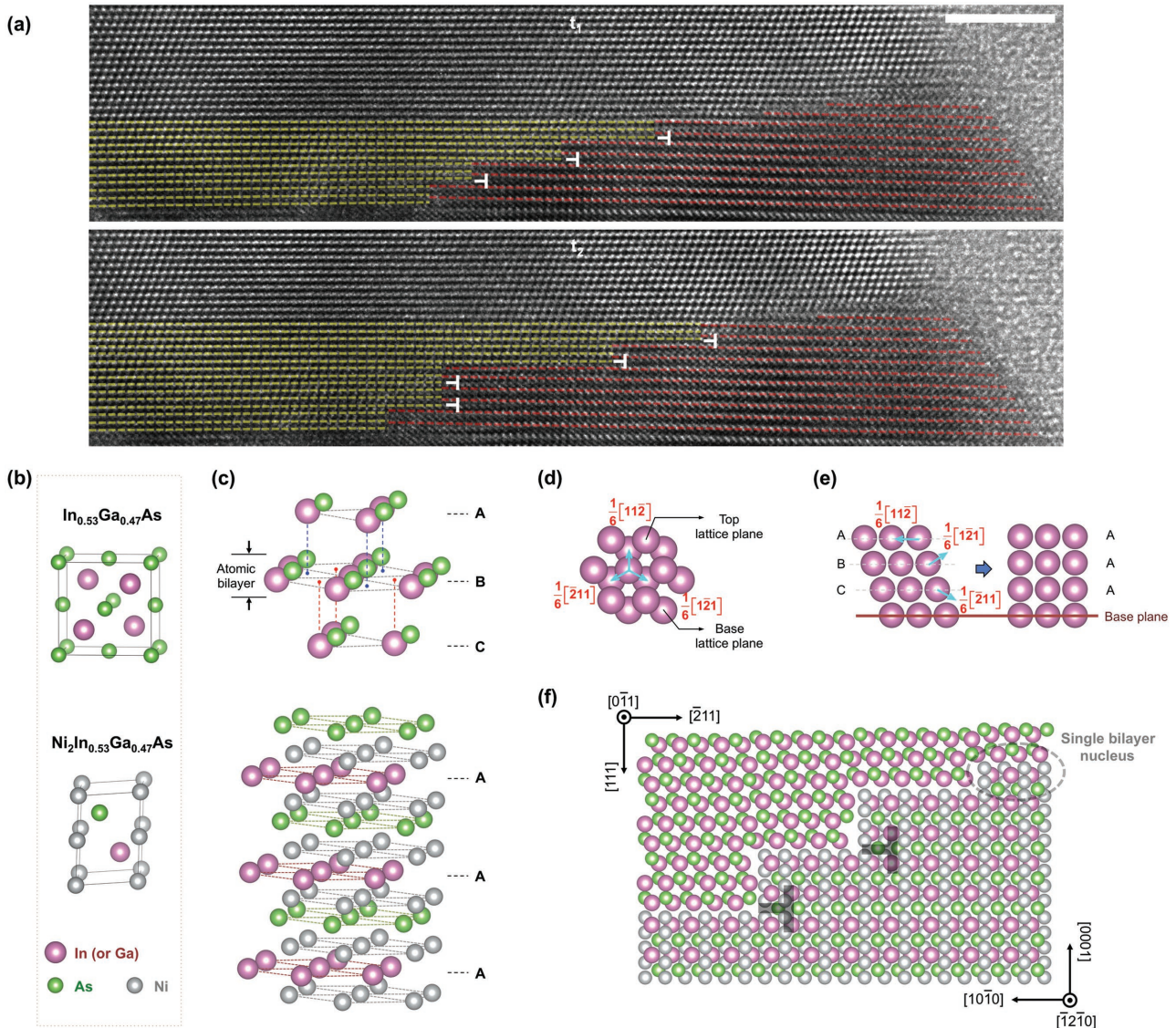


Figure 3. Atomic models that reveal the formation of interfacial disconnections during $\text{In}_{0.53}\text{Ga}_{0.47}\text{As}$ to $\text{Ni}_2\text{In}_{0.53}\text{Ga}_{0.47}\text{As}$ phase transformation. a) HRTEM images extracted from two separate time-instant in Movie S2 in the Supporting Information, giving an even closer look at the $\text{In}_{0.53}\text{Ga}_{0.47}\text{As}/\text{Ni}_2\text{In}_{0.53}\text{Ga}_{0.47}\text{As}$ interface. Scale bar is 5 nm. b) Lattice structures of $\text{In}_{0.53}\text{Ga}_{0.47}\text{As}$ (zinc blende) and $\text{Ni}_2\text{In}_{0.53}\text{Ga}_{0.47}\text{As}$ (simple hexagonal). c) Atomic arrangements in $\text{In}_{0.53}\text{Ga}_{0.47}\text{As}$ (with $[111]$ direction pointing upward) and $\text{Ni}_2\text{In}_{0.53}\text{Ga}_{0.47}\text{As}$ (with $[0001]$ direction pointing upward) respectively. In $\text{In}_{0.53}\text{Ga}_{0.47}\text{As}$ crystal, the atomic layers stack in an A-B-C-A-B-C... manner, while in $\text{Ni}_2\text{In}_{0.53}\text{Ga}_{0.47}\text{As}$ the stacking is A-A-A.... In $\text{In}_{0.53}\text{Ga}_{0.47}\text{As}$ crystal, an “atomic bilayer” usually refers to the bonded In (or Ga) monolayer and As monolayer. This is also used here for corresponding layers in $\text{Ni}_2\text{In}_{0.53}\text{Ga}_{0.47}\text{As}$ crystal after phase transformation. d) Top-view of two lattice planes in an A-B-C type of stacking, indicating that the top lattice plane has three possible in-plane gliding vectors in order to be overlapping with the bottom lattice plane. e) Side-view of how the A-B-C stacking of lattice planes shuffle into an A-A-A stacking manner by collective gliding of three lattice planes along three different gliding vectors as shown in (d). f) The reconstructed atomic structures at the interface in between $\text{In}_{0.53}\text{Ga}_{0.47}\text{As}$ (top left) and $\text{Ni}_2\text{In}_{0.53}\text{Ga}_{0.47}\text{As}$ (bottom right). The nature of single-bilayer nucleus and double-bilayer step height is depicted in this schematic, together with the labeled misfit dislocations. We removed one monolayer of As atoms at the interface of $\text{In}_{0.53}\text{Ga}_{0.47}\text{As}$ side, which overlaps with the Ni atoms in $\text{Ni}_2\text{In}_{0.53}\text{Ga}_{0.47}\text{As}$, in order to improve the clarity of this structure model at the interface region.

planes arrange in a A-B-C-A-B-C... manner (shown in Figure 3c), representing a typical fcc stacking. Along the $[0001]$ direction of $\text{Ni}_2\text{In}_{0.53}\text{Ga}_{0.47}\text{As}$ crystal, atomic planes arrange in an A-A-A... manner, which is due to the nature of its simple hexagonal lattice (different from typical hexagonal-close-packed (hcp) stacking). Therefore, during the phase transformation from $\text{In}_{0.53}\text{Ga}_{0.47}\text{As}$ to $\text{Ni}_2\text{In}_{0.53}\text{Ga}_{0.47}\text{As}$, the atomic bilayers need to glide in each atomic plane in order to transform from A-B-C... type of stacking into A-A-A... type

of stacking. Here, we simplified one atomic-bilayer into a lattice plane and depicted the gliding behaviors in Figure 3d,e. A top-view of the lattice planes is shown in Figure 3d, and the top lattice plane has three optional gliding directions to overlap with the bottom lattice plane, i.e., $\frac{1}{6}[11\bar{2}]$, $\frac{1}{6}[\bar{1}21]$, and $\frac{1}{6}[\bar{2}11]$, corresponding to three Shockley partial dislocations (also referred to as Shockley partials). From a side-view of the lattice planes as shown in Figure 3e, three lattice planes

need to glide collectively along one of the three Shockley partials in order to eliminate shear stress during phase transformation,^[51] as no external shear stress was applied to the NW. Therefore, a group of three (or multiples of three) atomic bilayers in In_{0.53}Ga_{0.47}As crystal will move all together by the collective gliding of three Shockley partials with a height of 3d₍₁₁₁₎ = 10.17 Å which is nearly equivalent to the height of double-bilayer ledge (2d₍₀₀₀₁₎ = 10.20 Å) in Ni₂In_{0.53}Ga_{0.47}As crystal with residual strain ≤0.3%. This also introduces one misfit-dislocation for each double-bilayer ledge. Finally, the atomic arrangement at the disconnection interface is reconstructed in Figure 3f, and both, the single-bilayer nucleus and the double-bilayer ledges are illustrated in the schematic.

Ledges with multilayer height have also been observed during in situ TEM in other nanowire systems, such as metal-catalyzed growth of Si^[52] and GaN^[53] nanowires, and phase transformation in InAs nanowire^[54] (from wurtzite to zinc-blende). During the metal-catalyzed nanowire growth, the growth species diffuse through the catalyst, supersaturate at the catalyst/nanowire interface, and generate new ledges on the interfacial plane. Since the catalyst has no epitaxial correlation to the nanowire, the number of layers in a ledge largely depends on the supersaturation rate^[52,55,56] or the property of nanowire material itself.^[53] In the phase transformation of InAs nanowire from wurtzite to zinc-blende phase,^[54] the atomic planes changed from A-B-A-B... (hcp) type of stacking to A-B-C... (fcc) type of stacking without elastic strain as the stoichiometry of the InAs and the size of its unit cell are conserved in this phase change. Ledges contained six bilayers by collectively gliding of three Shockley partials that each associated with two atomic bilayers in both the wurtzite and the zinc-blende phases. In our material system of In_{0.53}Ga_{0.47}As/Ni₂In_{0.53}Ga_{0.47}As, the phase transformation not only caused an unusual change in atomic stacking (A-B-C... type to A-A-A... type), but also introduced large elastic strain near the interfaces. Therefore, we observed a fixed ledge height of two bilayers in Ni₂In_{0.53}Ga_{0.47}As (three bilayers in In_{0.53}Ga_{0.47}As) and a misfit dislocation associated with the ledge unit. Our observations expound a new type of ledge formation and movement behaviors during contact metallization, that is the phase transformation with large elastic strain in nanowire channels, which serves as a direct proof and in fact the first observation of the applicability of the disconnection theory in nanoscale phase transformation.

We finally provide a qualitative analysis of the nickelide phase nucleation based on thermodynamic and kinetic grounds. This is to explain why the Ni₂In_{0.53}Ga_{0.47}As phase nucleated near the top of the nanowire channel where In_{0.53}Ga_{0.47}As interfaced with SiO₂ layer (as shown in Figure 2d), as opposed to the trimethylaluminum (TMA) treated HfO₂/In_{0.53}Ga_{0.47}As interface. As shown in **Figure 4a**, there are three possible nucleation sites: ① heterogeneous nucleation site near the nanowire top surface, where In_{0.53}Ga_{0.47}As interfaces with SiO₂ cap layer, ② homogeneous nucleation site inside the nanowire channel on the In_{0.53}Ga_{0.47}As/nickelide interfacial plane, and ③ heterogeneous nucleation site near the nanowire base, where In_{0.53}Ga_{0.47}As interfaces with HfO₂. Considering the classical case with a disc shaped nucleus (Section V, Supporting Information), the ratio of energy barriers between

heterogeneous (truncated disc) and homogeneous (full disc) nuclei is:

$$\frac{\Delta G_{\text{hetero}}^*}{\Delta G_{\text{homo}}^*} = \frac{\theta - \sin \theta \cos \theta}{\pi} \quad (1)$$

where θ is the contact angle of heterogeneous nucleus with the In_{0.53}Ga_{0.47}As/oxide interface.

Figure 4b schematically illustrates the relation between system free energy and the radius of nucleus, for both homogeneous and heterogeneous cases. The energy barrier for heterogeneous nucleation could be much smaller than the homogeneous nucleation, and the ratio of $\Delta G_{\text{hetero}}^*/\Delta G_{\text{homo}}^*$ depends on the contact angle θ as can be deduced from Equation (1). $\Delta G_{\text{hetero}}^*/\Delta G_{\text{homo}}^*$ is plotted in Figure 4c. In order to determine the ratio of $\Delta G_{\text{hetero}}^*/\Delta G_{\text{homo}}^*$, one needs to know each value of the interfacial energies that determine the contact angle θ . However, most of the interfacial energies ($\gamma_{\text{nickelide/oxide}}$ and $\bar{\gamma}$) for the In_xGa_{1-x}As system were not measured nor calculated to date. Despite this, we can hypothesize a value for θ by considering the possible shape of nucleus as shown in Figure 4d,e. We argue that the critical nucleus is preferred to form on coherent interfaces with a shape that is determined by the low energy facets.^[57] In our in situ studies at the temperature range of 280–350 °C, we observed clear facet selectivity of In_{0.53}Ga_{0.47}As (111) on which the Ni₂In_{0.53}Ga_{0.47}As phase preferred to grow. Therefore, it's reasonable to speculate that within our studied kinetic regime, the nucleated Ni₂In_{0.53}Ga_{0.47}As phase should be bound by other equivalent {111} facets as shown in Figure 4e. If we consider the other side at the interface, Ni₂In_{0.53}Ga_{0.47}As phase has a hexagonal lattice structure in which {1100} are the typically preferred low energy facets.^[58,59] Both of these two facet-groups enclose an equivalent hexagonal boundary for the critical nucleus. At the same time, studies of silicide formation in Si nanowires informed that the silicide/oxide interface usually had a larger interfacial energy than Si/SiO₂ interface, resulting in a contact angle $\theta > 90^\circ$.^[33] Therefore, for a reasonably speculated contact angle of 120° in the In_{0.53}Ga_{0.47}As/Ni₂In_{0.53}Ga_{0.47}As system under our experimental conditions, the ratio of nucleation barrier is $\Delta G_{\text{hetero}}^*/\Delta G_{\text{homo}}^* = 0.64$ (labeled in Figure 4c), which is within a typical range of ratios that was found for the more studied silicide growth.^[31,60] This indicates the thermodynamic preference of heterogeneous nucleation, but does not account for kinetic considerations. For this, we need to consider the nucleation rate, which can be characterized as:

$$R = \omega C \exp\left(-\frac{\Delta G_D}{kT}\right) \exp\left(-\frac{\Delta G^*}{kT}\right) \quad (2)$$

where ω is frequency related to atomic vibrations, C is the concentration of critical sized nucleus, ΔG_D is the activation energy for Ni atoms to diffuse to the reaction interface, and ΔG^* is the energy barrier for nucleus. By invoking known values into equation (4), (Section V, Supporting Information), we can get:

$$\frac{R_{\text{hetero}}}{R_{\text{homo}}} \approx 1.26 \exp\left(\frac{\Delta G_{\text{homo}}^* - \Delta G_{\text{hetero}}^*}{kT}\right) \quad (3)$$

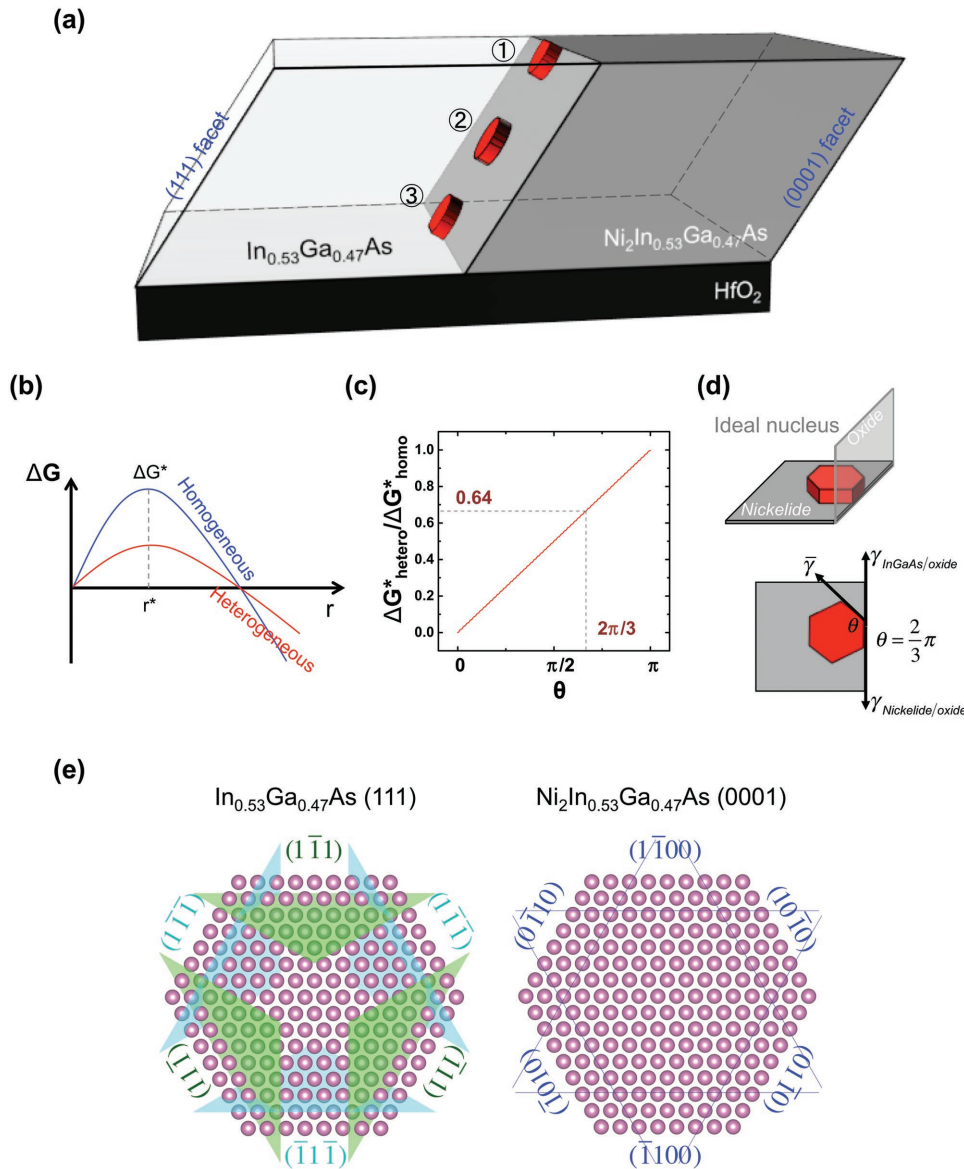


Figure 4. Nucleation model of the nickelide reaction in the [011] oriented $\text{In}_{0.53}\text{Ga}_{0.47}\text{As}$ nanowire channel. a) Schematics of the three possible nucleation sites for nickelide phase on the $\text{In}_{0.53}\text{Ga}_{0.47}\text{As}$ /nickelide interface, which are ① heterogeneous nucleation site at $\text{In}_{0.53}\text{Ga}_{0.47}\text{As}$ /nickelide/ SiO_2 triple phase boundary (TPB), ② homogeneous nucleation site at $\text{In}_{0.53}\text{Ga}_{0.47}\text{As}$ /nickelide/ HfO_2 TPB, and ③ heterogeneous nucleation site at $\text{In}_{0.53}\text{Ga}_{0.47}\text{As}$ /nickelide/ HfO_2 TPB. b) Plot of free energy of a nucleus as a function of radius for both homogeneous and heterogeneous cases according to the derived thermodynamic model (Section V, Supporting Information). c) The ratio of energy barriers $\Delta G^*_{\text{hetero}}/\Delta G^*_{\text{homo}}$ as a function of contact angle of the nucleus at the interface of $\text{In}_{0.53}\text{Ga}_{0.47}\text{As}$ /dielectric as showing in (b). d) A hypothesized shape of heterogeneous nucleus that shows a hexagonal shape. This hexagonal disc is not necessarily equilateral and may contain small facet steps, while the contact angle will be fixed at $\theta = 2\pi/3$ that corresponds to the ratio $\Delta G^*_{\text{hetero}}/\Delta G^*_{\text{homo}} = 0.64$ in (c). (d) An ideal heterogeneous nucleus that shows a hexagonal shape from side and top views. e) The reason for the hypothesized hexagonal nucleus is illustrated by the atomic arrangements at the $\text{In}_{0.53}\text{Ga}_{0.47}\text{As}$ (111) || $\text{Ni}_2\text{In}_{0.53}\text{Ga}_{0.47}\text{As}$ (0001) interface, enclosed by the low-energy facets for both sides of the interface.

Therefore, the nucleation rate is also directly related to the nucleation barrier. Since the nucleation barrier ΔG^*_{homo} is about few electron-volts (eV) for a typical metallization process in nanowires,^[33,60] the estimated ratio of nucleation rate $R_{\text{hetero}}/R_{\text{homo}} \geq 1.5 \times 10^6$. This analysis corroborate our experimental observations that the heterogeneous nucleation is much more favorable both thermodynamically and kinetically.

There are two types of heterogeneous nucleation sites in our model (② and ③ in Figure 4a), which are at the interface

with SiO_2 top or with HfO_2 bottom layers. This HfO_2 layer was grown on $\text{In}_{0.53}\text{Ga}_{0.47}\text{As}$ by atomic layer deposition (ALD) with a pretreatment of five-cycle consecutive pulses of TMA and H_2 plasma. This surface pretreatment was found to introduce an intermediate Al layer and enhance the bonding strength between $\text{In}_{0.53}\text{Ga}_{0.47}\text{As}$ and HfO_2 by forming As–Al–As bonds and Al–O bond on each side respectively (Section VI, Supporting Information).^[61,62] It is expected that the abundance of dangling bonds and vacant sites at the sputtered SiO_2 layer on $\text{In}_{0.53}\text{Ga}_{0.47}\text{As}$

(as opposed to ALD deposited HfO_2) will enhance the diffusion of Ni at that interface since Ni is known to diffuse through interstitial states.^[63] We believe that this improved bonding strength between $\text{In}_{0.53}\text{Ga}_{0.47}\text{As}$ and HfO_2 reduces the diffusion rate of Ni at this interface and increases the ΔG_D in Equation (2), resulting in a reduced nucleation rate. One should not exclude the possibility that the bonding strength increases the elastic strain E_{strain} if $\text{Ni}_2\text{In}_{0.53}\text{Ga}_{0.47}\text{As}$ nucleates at the $\text{In}_{0.53}\text{Ga}_{0.47}\text{As}/\text{HfO}_2$ interface and then increases the nucleation barrier according to Equation S8 (Supporting Information). Therefore, we believe that the coordinated bonding between $\text{In}_{0.53}\text{Ga}_{0.47}\text{As}$ and HfO_2 limits the heterogeneous nucleation at this interface. Moreover, though the $\text{In}_{0.53}\text{Ga}_{0.47}\text{As}$ nanowire is also covered by SiO_2 on the sides, we believe that once $\text{Ni}_2\text{In}_{0.53}\text{Ga}_{0.47}\text{As}$ nucleated from the top surface the fast diffusion of Ni along the sidewalls would only contribute to the ledge propagations by nucleating at the kink sites on the train of ledges instead of nucleating new ledges.

3. Conclusions

In summary, we carried out in situ heating TEM experiments to study the contact metallization process in between Ni contact and $\text{In}_{0.53}\text{Ga}_{0.47}\text{As}$ nanowire channels, and observed the detailed ledge formation and movement behaviors at atomic resolution. We found that the reacted interface followed the $\text{In}_{0.53}\text{Ga}_{0.47}\text{As}$ (111) || $\text{Ni}_2\text{In}_{0.53}\text{Ga}_{0.47}\text{As}$ (0001) atomic plane, and the ledges nucleated as a train of strained single-bilayers. Once the strain energy in single-bilayer ledges was relieved in part by forming misfit dislocations, their velocity decreased permitting the formation of associated single-bilayer ledges, the double-bilayer ledges. Consequently, these nickelide ledges moved with a double-bilayer height that became the unit height of ledges in this phase transformation. Our atomic models depicted the ledge propagation behaviors that are related to collective gliding of three $\text{In}_{0.53}\text{Ga}_{0.47}\text{As}$ single-bilayers along three Shockley partials to cancel out the shear stress during phase transformation. Our analysis for the nucleation of new ledges indicates that the heterogeneous nucleation at the nanowire top surface is favored both kinetically and thermodynamically and is in good agreement with our experimental observations. Our in situ studies demonstrated for the first time the applicability of interfacial disconnection theory in contact metallization for compound semiconductor nanoscale channels.

4. Experimental Section

Fabrication of InGaAs Nanowire Channels on Insulator on Top of Si Substrate: In this work, a 50 nm thin undoped $\text{In}_{0.53}\text{Ga}_{0.47}\text{As}$ film (MBE grown on (001) InP by Intelligent Epitaxy Inc., Richardson, Texas) was first transferred on insulator on Si substrate with a solid-state wafer bonding process that was developed previously and reported elsewhere.^[45,46] After the transfer, the stacking layers from top to bottom were 50 nm $\text{In}_{0.53}\text{Ga}_{0.47}\text{As}$, 15 nm HfO_2 , 200 nm SiO_2 , NiSi_x bonding layer (average thickness $\approx 200\text{nm}$), and 500 μm Si substrate. Second, 30 nm wide horizontal nanowire

structures were patterned on top of the $\text{In}_{0.53}\text{Ga}_{0.47}\text{As}$ layer utilizing a 100 kV e-beam writer (JEOL JBX-6300FS) with beam size $\approx 8\text{ nm}$. The arrangement of patterned nanowires is schematically shown in Figure 1a (also see details in Figure S1, Supporting Information), which is to ensure that one nanowire was captured within a single FIB milled lamellae along the x-direction (see details in Section I, Supporting Information).

Specimen Lamellae Preparation by FIB Milling and In Situ Lift-Out (INLO): TEM specimens in this work were prepared by FIB milling on the samples of $\text{In}_{0.53}\text{Ga}_{0.47}\text{As}$ nanowire on insulator on Si substrate. Prior to FIB milling, 400 nm SiO_2 and 50 nm Pt were deposited atop the sample to prevent damage of interested area under ion beams. SiO_2 layer was deposited at a low temperature (100 °C) by plasma enhanced chemical vapor deposition to prevent any possible reaction between Ni contact and $\text{In}_{0.53}\text{Ga}_{0.47}\text{As}$ nanowires prior to our in situ heating experiments. The FIB and INLO process utilized here, as shown in Figure S2 (Supporting Information) first row, followed conventional procedures^[64,65] in which a 30 kV Ga beam was used for rough milling and reduced voltage (10 kV) was used for fine milling.

Transferring Specimen Lamellae on Top of Thermal E-Chips: The process to transfer FIB lamellae onto the TEM window of a thermal E-chip (AHA chip, Protochips Inc.) was shown in Figure S2 (Supporting Information), second row. The TEM window was made of conductive ceramic with many manmade circular holes for electron-beam transparency. A larger rectangular hole was drilled intentionally for better imaging of the FIB lamellae for the HRTEM video recording of the reaction dynamics. Two Pt posts were also deposited on the edge of the opening region (shown in Figure S2 step 4, Supporting Information) to hold the transferred FIB lamellae. These two Pt posts not only helped maintaining the flatness of specimen lamellae during transfer, but also facilitated the further thinning and cleaning steps by lifting up the lamellae from the surface of ceramic membrane. Finally, the transferred specimen lamellae was further thinned with FIB with reduced voltage (10 kV), until the lamellae reached a thickness $\approx 60\text{ nm}$.

In Situ TEM Movies Recording: In this study, TEM was operated at 300 kV with minimal electron dose that could still maintain clear imaging at highest magnification ($\times 1\text{ M}$). The electron beam was blocked during the in situ heating experiments except for imaging and video recording for 1–2 min. The electron beam was never focused on the interested area of the specimen in order to minimize the possible damages induced by electron beam. For over 10 samples that were studied in this work, no noticeable beam effect was observed during the phase transformation from InGaAs to nickelide (detailed discussions in Section II, Supporting Information). HRTEM images were extracted from the video frames, and processed in the DigitalMicrograph software where diffraction spots were masked and then inverted to enhance the image clarity. A list of the supporting movies is provided below:

Movie S1: Low-magnification TEM recording of nickelide reactions in a [110] oriented $\text{In}_{0.53}\text{Ga}_{0.47}\text{As}$ nanowire in which $\text{In}_{0.53}\text{Ga}_{0.47}\text{As}/\text{nickelide}$ interface shows a slanted profile corresponding to $\text{In}_{0.53}\text{Ga}_{0.47}\text{As}$ (111)// $\text{Ni}_2\text{In}_{0.53}\text{Ga}_{0.47}\text{As}$ (0001). This reaction evolved at 320 °C, and the video was recorded at 25 frames s^{-1} , and speeded up $\times 2$.

Movie S2: High-resolution TEM recording of nickelide reactions in a [110] oriented $\text{In}_{0.53}\text{Ga}_{0.47}\text{As}$ nanowire in which nickelide phase nucleated at the top surface of nanowire

channel and the ledges moved on the interface of $\text{In}_{0.53}\text{Ga}_{0.47}\text{As}$ (111)// $\text{Ni}_2\text{In}_{0.53}\text{Ga}_{0.47}\text{As}$ (0001). This reaction evolved at 300 °C, and the video was recorded at 25 frames s^{-1} .

Movie S3: Another High-resolution TEM recording on the same sample as in Movie S2 and at the same reaction temperature, but in a different time duration.

Nickelide Phase Identification: Recent studies on planar nickelide reactions had identified a sequential formation of $\text{Ni}_3\text{In}_{0.53}\text{Ga}_{0.47}\text{As}$, $\text{Ni}_2\text{In}_{0.53}\text{Ga}_{0.47}\text{As}$, and NiAs with temperatures.^[43] Here, the nickelide phase was concluded as $\text{Ni}_2\text{In}_{0.53}\text{Ga}_{0.47}\text{As}$ due to the following reasons: (1) the study was carried out at temperatures lower than the decomposition temperature of the nickelide phase, and therefore out-diffusion of In and Ga (which lead to the formation of NiAs phase) was not favoured. (2) 230 °C was the onset temperature of nickelide reaction in the studies and in most of the other studies.^[40] However, in ref. ^[43], the onset was 300 °C which indicated a temperature offset and placed the in situ experiments on the higher end of the temperatures where $\text{Ni}_3\text{In}_{0.53}\text{Ga}_{0.47}\text{As}$ phase was observed. (3) The nickelide lattice constants were measured in a region far from the reaction interface (i.e., strain-free), and the lattice constants were in agreement with those of $\text{Ni}_2\text{In}_{0.53}\text{Ga}_{0.47}\text{As}$ that were obtained in a prior study on planar structures.^[41] (4) These lattice constants did not fit in the range of values reported in the temperature-dependent nickelide phases in ref. ^[43] in which the different surrounding layers (InP substrate and TiN cap layer) might play a role. (5) As shown in Figure 3b, the nickelide phase had a hexagonal lattice structure with Ni atoms occupying the corner sites (0,0,0) and the edge sites (0,0,1/2). In (or Ga) atoms and As atoms occupied the (1/3,2/3,3/4) site and the (2/3,1/3,1/4) site, respectively. This corresponded to the stoichiometry of $\text{Ni}_2\text{In}_{0.53}\text{Ga}_{0.47}\text{As}$. There were still another two empty sites (1/3,2/3,1/4) and (2/3,1/3,3/4) that Ni could selectively occupy, resulting in a higher Ni-stoichiometry of $\text{Ni}_3\text{In}_{0.53}\text{Ga}_{0.47}\text{As}$. This sounded reasonable from a pure structural aspect, but was not energy favored in the phase transformation that was observed in this work. As illustrated in Figure 3, Ni atoms diffused in between the In (or Ga) and As atomic planes to form the nickelide phase, and the formed nickelide phase has a smaller in-plane lattice constant than that in $\text{In}_{0.53}\text{Ga}_{0.47}\text{As}$. If indeed $\text{Ni}_3\text{In}_{0.53}\text{Ga}_{0.47}\text{As}$ phase formed, there would have been more Ni “squeezing” in between the already close-packed In or As atomic planes, which is inconsistent with the smaller in-plane lattice constant after phase the transformation.

Supporting Information

Supporting Information is available from the Wiley Online Library or from the author.

Acknowledgements

The fabrication and structural characterization were performed at the Center for Integrated Nanotechnologies (CINT), a U.S. Department of Energy Office of Basic Energy Sciences user facility at Los Alamos National Laboratory (Contract DE-AC52-06NA25396) and

Sandia National Laboratories (Contract DE-AC04-94AL85000) through a CINT user proposal. The authors would like to acknowledge discussions with Drs. Nan Li, Wei Tang, Katherine L. Jungjohann, William M. Mook, Jinkyong Yoo, and Ms. Ren Liu, as well as discussions and technical supports from John Nogan, Anthony R. James, Douglas V. Pete, Denise B. Webb, and Willard Ross of Sandia National Laboratories. S.A.D. thanks NSF support for R.C. under DMR-1503595, and partially from ECCS-1351980.

Conflict of Interest

The authors declare no conflict of interest.

- [1] Y. Cui, C. M. Lieber, *Science* **2001**, *291*, 851.
- [2] X. Duan, Y. Huang, Y. Cui, J. Wang, C. M. Lieber, *Nature* **2001**, *409*, 66.
- [3] Y. Huang, X. Duan, Y. Cui, L. J. Lauhon, K.-H. Kim, C. M. Lieber, *Science* **2001**, *294*, 1313.
- [4] Y. Huang, X. Duan, Q. Wei, C. M. Lieber, *Science* **2001**, *291*, 630.
- [5] D. Hisamoto, W.-C. Lee, J. Kedzierski, H. Takeuchi, K. Asano, C. Kuo, E. Anderson, T.-J. King, J. Bokor, C. Hu, *IEEE Trans. Electron Devices* **2000**, *47*, 2320.
- [6] M. Jeong, B. Doris, J. Kedzierski, K. Rim, M. Yang, *Science* **2004**, *306*, 2057.
- [7] I. Ferain, C. A. Colinge, J.-P. Colinge, *Nature* **2011**, *479*, 310.
- [8] S. A. Dayeh, D. P. Aplin, X. Zhou, P. K. Yu, E. T. Yu, D. Wang, *Small* **2007**, *3*, 326.
- [9] S. A. Dayeh, D. Susac, K. L. Kavanagh, E. T. Yu, D. Wang, *Nano Lett.* **2008**, *8*, 3114.
- [10] S. A. Dayeh, C. Soci, X.-Y. Bao, D. Wang, *Nano Today* **2009**, *4*, 347.
- [11] M. S. Gudiksen, L. J. Lauhon, J. Wang, D. C. Smith, C. M. Lieber, *Nature* **2002**, *415*, 617.
- [12] C. J. Barrelet, A. B. Greytak, C. M. Lieber, *Nano Lett.* **2004**, *4*, 1981.
- [13] R. Yan, D. Gargas, P. Yang, *Nat. Photonics* **2009**, *3*, 569.
- [14] Y. Wu, J. Xiang, C. Yang, W. Lu, C. M. Lieber, *Nature* **2004**, *430*, 61.
- [15] F. Léonard, A. A. Talin, *Nat. Nanotechnol.* **2011**, *6*, 773.
- [16] R. Requist, P. P. Baruselli, A. Smogunov, M. Fabrizio, S. Modesti, E. Tosatti, *Nat. Nanotechnol.* **2016**, *11*, 499.
- [17] W. Tang, S. A. Dayeh, S. T. Picraux, J. Y. Huang, K.-N. Tu, *Nano Lett.* **2012**, *12*, 3979.
- [18] J. Appenzeller, J. Knoch, E. Tutuc, M. Reuter, S. Guha, *Electron Devices Meeting (IEDM)* **2006**, 1.
- [19] Y. Chen, Y.-C. Lin, X. Zhong, H.-C. Cheng, X. Duan, Y. Huang, *Nano Lett.* **2013**, *13*, 3703.
- [20] Y. Chen, Y.-C. Lin, C.-W. Huang, C.-W. Wang, L.-J. Chen, W.-W. Wu, Y. Huang, *Nano Lett.* **2012**, *12*, 3115.
- [21] J. Tang, C.-Y. Wang, F. Xiu, Y. Zhou, L.-J. Chen, K. L. Wang, *Adv. Mater. Sci. Eng.* **2011**, *2011*, 316513.
- [22] W. Tang, B.-M. Nguyen, R. Chen, S. A. Dayeh, *Semicond. Sci. Technol.* **2014**, *29*, 054004.
- [23] H. Saka, T. Kamino, S. Ara, K. Sasaki, *MRS Bull.* **2008**, *33*, 93.
- [24] N. Petkov, *ISRN Nanotechnol.* **2013**, *2013*, 893060.
- [25] H. Zheng, Y. S. Meng, Y. Zhu, *MRS Bull.* **2015**, *40*, 12.
- [26] R. Boston, Z. Schnepp, Y. Nemoto, Y. Sakka, S. R. Hall, *Science* **2014**, *344*, 623.
- [27] S.-C. Wang, M.-Y. Lu, A. Manekathodi, P.-H. Liu, H.-C. Lin, W.-S. Li, T.-C. Hou, S. Gwo, L.-J. Chen, *Nano Lett.* **2014**, *14*, 3241.
- [28] F. Panciera, Y. C. Chou, M. C. Reuter, D. Zakharov, E. A. Stach, S. Hofmann, F. M. Ross, *Mater. Mater* **2015**, *14*, 820.
- [29] Q. Yu, M.-M. Mao, Q.-J. Li, X.-Q. Fu, H. Tian, J.-X. Li, S. X. Mao, Z. Zhang, *Nano Lett.* **2016**, *16*, 1156.

- [30] V. T. Fauske, J. Huh, G. Divitini, D. L. Dheeraj, A. M. Munshi, C. Ducati, H. Weman, B.-O. Fimland, A. T. J. van Helvoort, *Nano Lett.* **2016**, *16*, 3051.
- [31] W. Tang, S. T. Picraux, J. Y. Huang, A. M. Gusak, K.-N. Tu, S. A. Dayeh, *Nano Lett.* **2013**, *13*, 2748.
- [32] W. Tang, S. T. Picraux, J. Y. Huang, X. Liu, K.-N. Tu, S. A. Dayeh, *Nano Lett.* **2013**, *13*, 6009.
- [33] Y.-C. Chou, W.-W. Wu, L.-J. Chen, K.-N. Tu, *Nano Lett.* **2009**, *9*, 2337.
- [34] R. Chen, K. L. Jungjohann, W. M. Mook, J. Nogan, S. Dayeh, *Nano Lett.* **2017**, *17*, 2189.
- [35] J. A. Del Alamo, *Nature* **2011**, *479*, 317.
- [36] E. Kuphal, *J. Cryst. Growth* **1984**, *67*, 441.
- [37] S. Kim, M. Yokoyama, N. Taoka, R. Iida, S. Lee, R. Nakane, Y. Urabe, N. Miyata, T. Yasuda, H. Yamada, *Electron Devices Meeting (IEDM)* **2010**, 26.6.1.
- [38] X. Zhang, H. X. Guo, X. Gong, Q. Zhou, Y.-C. Ye, *J. Electrochem. Soc.* **2012**, *159*, H511.
- [39] M. Abraham, S.-Y. Yu, W. H. Choi, R. T. Lee, S. E. Mohny, *J. Appl. Phys.* **2014**, *116*, 164506.
- [40] L. Czornomaz, M. El Kazzi, M. Hopstaken, D. Caimi, P. Machler, C. Rossel, M. Bjoerk, C. Marchiori, H. Siegwart, J. Fompeyrine, *Solid-State Electron.* **2012**, *74*, 71.
- [41] Ivana, Y. Lim Foo, X. Zhang, Q. Zhou, J. Pan, E. Kong, M. H. Samuel Owen, Y.-C. Ye, *J. Vac. Sci. Technol., B* **2013**, *31*, 012202.
- [42] P. Shekhter, S. Mehari, D. Ritter, M. Eizenberg, *J. Vac. Sci. Technol., B* **2013**, *31*, 031205.
- [43] S. Zhiou, T. Nguyen-Thanh, P. Rodriguez, F. Nemouchi, L. Rapenne, N. Blanc, N. Boudet, P. Gergaud, *J. Appl. Phys.* **2016**, *120*, 135304.
- [44] C. Perrin, E. Ghegin, S. Zhiou, F. Nemouchi, P. Rodriguez, P. Gergaud, P. Maugis, D. Mangelinck, K. Hoummada, *Appl. Phys. Lett.* **2016**, *109*, 131902.
- [45] R. Chen, S. A. Dayeh, *Nano Lett.* **2015**, *15*, 3770.
- [46] X. Dai, B. M. Nguyen, Y. Hwang, C. Soci, S. A. Dayeh, *Adv. Funct. Mater.* **2014**, *24*, 4420.
- [47] In InGaAs crystal, an “atomic bilayer” usually refers to the bonded In (or Ga) monolayer and As monolayer. This name is also used here in this manuscript for corresponding layers in nickelide crystal after phase transformation.
- [48] J. P. Hirth, *J. Phys. Chem. Solids* **1994**, *55*, 985.
- [49] J. Hirth, *Metall. Mater. Trans. A* **1994**, *25*, 1885.
- [50] J. P. Hirth, R. G. Hoagland, R. J. Kurtz, *Metall. Mater. Trans. A* **1998**, *29*, 2033.
- [51] N. Li, S. K. Yadav, J. Wang, X.-Y. Liu, A. Misra, *Sci. Rep.* **2015**, *5*, 18554.
- [52] S. Hofmann, R. Sharma, C. T. Wirth, F. Cervantes-Sodi, C. Ducati, T. Kasama, R. E. Dunin-Borkowski, J. Drucker, P. Bennett, J. Robertson, *Nat. Mater.* **2008**, *7*, 372.
- [53] A. D. Gamalski, J. Tersoff, E. A. Stach, *Nano Lett.* **2016**, *16*, 2283.
- [54] H. Zheng, J. Wang, J. Y. Huang, J. Wang, Z. Zhang, S. X. Mao, *Nano Lett.* **2013**, *13*, 6023.
- [55] C. Y. Wen, J. Tersoff, M. C. Reuter, E. A. Stach, F. M. Ross, *Phys. Rev. Lett.* **2010**, *105*, 195502.
- [56] H. Cui, Y. Y. Lü, G. W. Yang, Y. M. Chen, C. X. Wang, *Nano Lett.* **2015**, *15*, 3640.
- [57] D. A. Porter, K. E. Easterling, M. Sherif, *Phase Transformations in Metals and Alloys* (Revised Reprint), CRC Press, Boca Raton, FL **2009**.
- [58] V. Pankoke, P. Kratzer, S. Sakong, *Phys. Rev. B* **2011**, *84*, 075455.
- [59] K. W. Ng, W. S. Ko, F. Lu, C. J. Chang-Hasnain, *Nano Lett.* **2014**, *14*, 4757.
- [60] Y.-C. Chou, W.-W. Wu, C.-Y. Lee, C.-Y. Liu, L.-J. Chen, K.-N. Tu, *J. Phys. Chem. C* **2011**, *115*, 397.
- [61] W. Melitz, J. Shen, T. Kent, A. C. Kummel, R. Droopad, *J. Appl. Phys.* **2011**, *110*, 013713.
- [62] G. Cai, Q. Sun, Y. Jia, E. Liang, *Mater. Sci. Semicond. Process.* **2016**, *41*, 1.
- [63] J. Ciccariello, S. Poize, P. Gas, *J. Appl. Phys.* **1990**, *67*, 3315.
- [64] L. A. Giannuzzi, B. W. Kempshall, S. M. Schwarz, J. K. Lomness, B. I. Prenitzer, F. A. Stevie, *Introduction to Focused Ion Beams*, Springer, **2005**, 201.
- [65] J. Mayer, L. A. Giannuzzi, T. Kamino, J. Michael, *MRS Bull.* **2007**, *32*, 400.

Received: December 12, 2016
Revised: April 6, 2017
Published online: June 8, 2017



Supporting Information

for *Small*, DOI: 10.1002/sml.201604117

Recordings and Analysis of Atomic Ledge and Dislocation
Movements in InGaAs to Nickelide Nanowire Phase
Transformation

*Renjie Chen** and *Shadi A. Dayeh**

Supporting Information for

Recordings and Analysis of Atomic Ledge and Dislocation Movements in InGaAs to Nickelide Nanowire Phase Transformation

Renjie Chen and Shadi A. Dayeh**

Mr. Renjie Chen

Department of Electrical and Computer Engineering, University of California San Diego, La Jolla,
California 92093, USA

E-mail: rec006@ucsd.edu

Prof. Shadi A. Dayeh

Department of Electrical and Computer Engineering; Materials Science and Engineering Program;
Department of NanoEngineering, University of California San Diego, La Jolla, California 92093,
USA

E-mails: sdayeh@ucsd.edu

Table of Contents

I. Integration of FIB lamellae onto TEM platform.....	2
II. Discussions of the potential beam-effects on our in-situ TEM observations	3
III. Original TEM images for Figure 2 & 3 in main text.....	4
IV. An estimation of the strain level before and after double-bilayer formation.....	5
V. Derivation of the nucleation model at nanowire/nickelide interface.....	7
VI. The profile of protruded nickelide phase at the reaction-front	9
References	11

I. Integration of FIB lamellae onto TEM platform

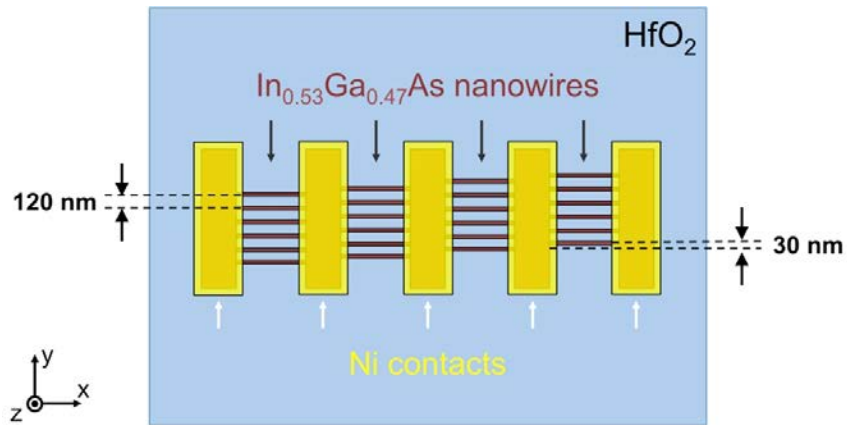
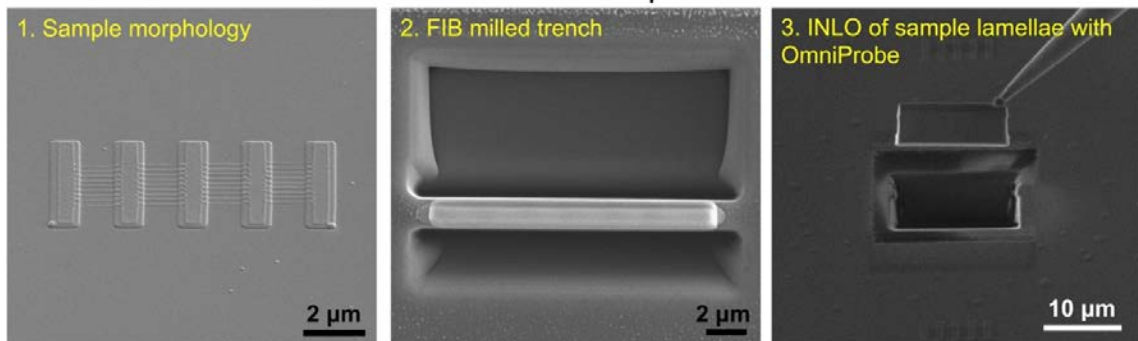


Figure S1. Schematic for the top view of $\text{In}_{0.53}\text{Ga}_{0.47}\text{As}$ nanowires arrangement. Each nanowire has a width of 30nm, and a center-to-center distance between two nanowires in a column to be 120nm. The column-to-column group offset was 30nm.

FIB Processes on Sample Substrate



FIB Processes on Thermal E-chips

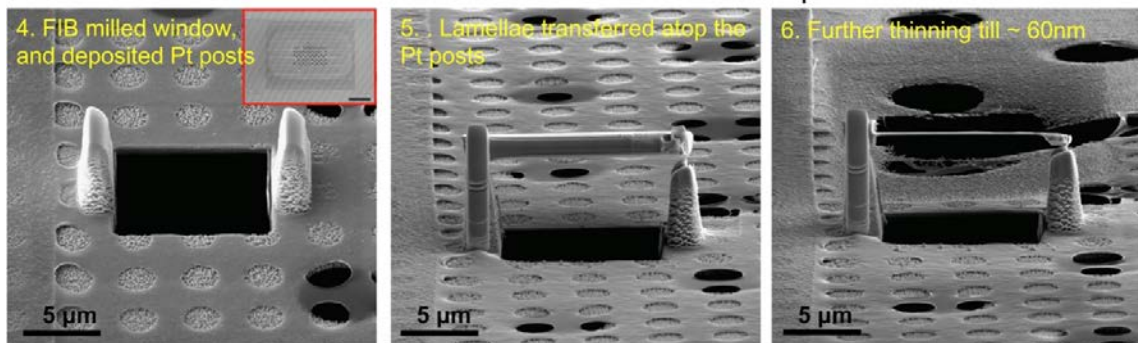


Figure S2. SEM images showing the sequences in FIB processes. The fabrication flow exhibits the sequences of transferring the FIB cut lamellae from the home substrate onto the TEM membrane window of a thermal E-chip. The inserted image in step 4 is the overview of TEM membrane with scale bar of 100 μm .

A TEM lamellae prepared by FIB milling usually has a final thickness about 60~80 nm, with positioning accuracy > 100 nm. Therefore, the nanowire arrangement needed to be smartly designed (shown in Figure S1) in order to have at least one intact nanowire channel that is fully embedded in the SiO₂ layer and appears in the FIB milled lamellae. The 120nm wire-to-wire distance in a column ensures no overlap of two nanowires in a FIB lamellae, and the 30nm column-to-column guarantees 2~3 nanowire channels remain along the FIB lamellae. If 3 nanowires remain, the center one would be the intact nanowire fully embedded by SiO₂ top layer, and the other two would be partially damaged by FIB on the sidewall. If 2 nanowires remain, both of them would be intact nanowires and the in-situ study could be focused on either on them.

II. Discussions of the potential beam-effects on our in-situ TEM observations

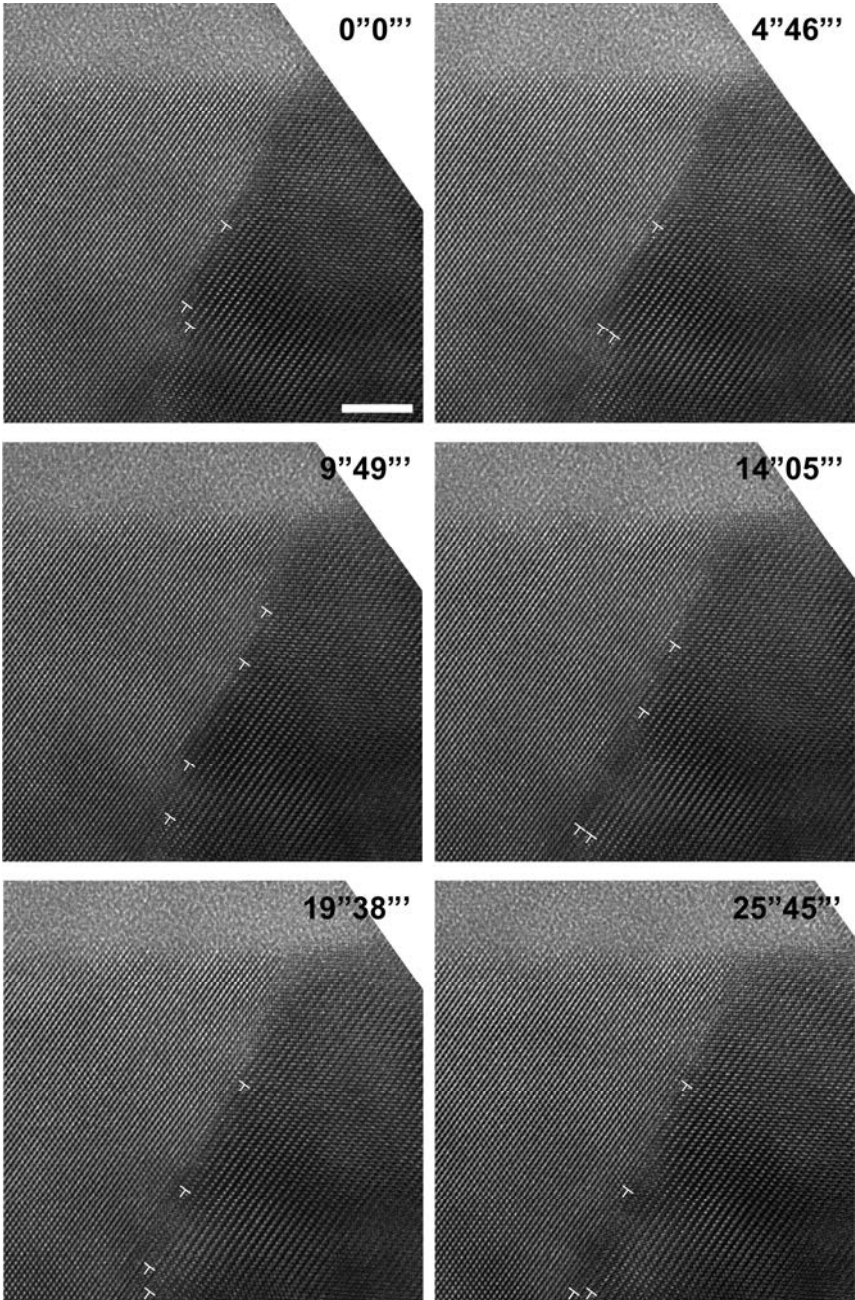
The incident beam in TEM carries energetic electrons that can interact with specimen materials through elastic and inelastic scatterings.¹ During these interactions, electrons may cause momentum change of specimen atoms, leading to atomic displacement and structural defects, or transfer energy to the specimen materials. The typically concerned beam effects during TEM imaging and recording include knock-on damage, beam-induced coalescence, and local heating.²

The knock-on damages are generally observed as defects (e.g. dislocations, voids, and bubbles) and structural changes (e.g. crystalline-to-amorphous or order-to-disorder phase transitions).³ In order to see these phenomena, most of the (electron or ion) irradiation studies were carried out under very high voltages (1~3 MV).⁴ Here in our in-situ study, the TEM system was operated at 300kV and a minimal electron dose for HRTEM imaging. The electron beam was never focused on the interested area of the specimen. Therefore, none of these beam-induced damages were observed.

Beam-induced coalescence and local heating effect are largely concerned for specimen in liquid phases,⁵ and reactions can be stimulated by electron-beam in liquid-cell TEM studies though energy transfer in between electron-beam and the specimen.^{6,7} However, in in-situ TEM studies of solid-state reactions (as in our case), such beam effects have not been found to influence the reaction under moderate imaging conditions.^{8,9} Though beam-heating may raise the local temperatures, calculations indicate only a small temperature rise (a few degrees or less) on solid specimens with good thermal conductivities.¹ This small temperature variations in a local area will be alter our observed phase transformations, as the nickelide phase was generally reported stable over a large temperature range (230 ~ 450 °C).¹⁰

Ex-situ reactions are generally used as a validation to exclude the beam effect.¹¹ In our prior ex-situ heating study,¹² the same nickelide phase ($\text{Ni}_2\text{In}_{0.53}\text{Ga}_{0.47}\text{As}$) was observed at a RTA temperature of 300 °C, in which however, no detailed ledge movement behaviors could be observed without in-situ observations. Therefore, we conclude that the reported InGaAs to nickelide phase transformation in this work was mainly dominated by the thermally driven Ni-InGaAs solid-state reaction, with negligible effect from the electron-beam irradiations.

III. Original TEM images for Figure 2 & 3 in main text



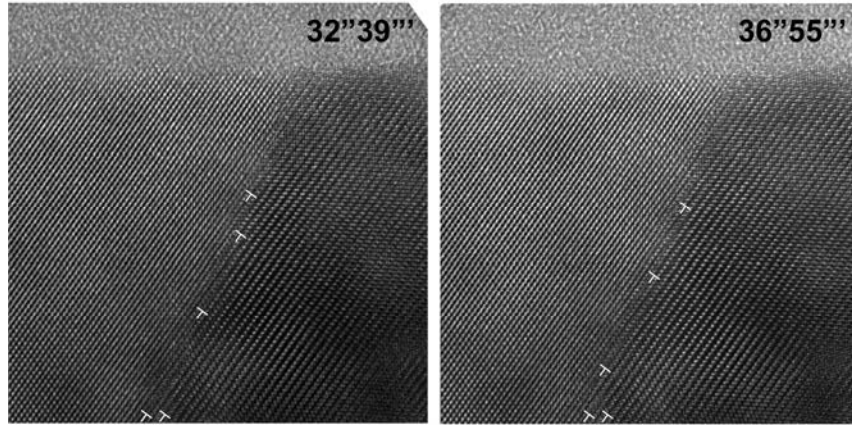


Figure S3. The original TEM images for Figure 2(d) in the main text without labeling of the atomic planes. All these HRTEM images share the same scale bar of 5 nm.

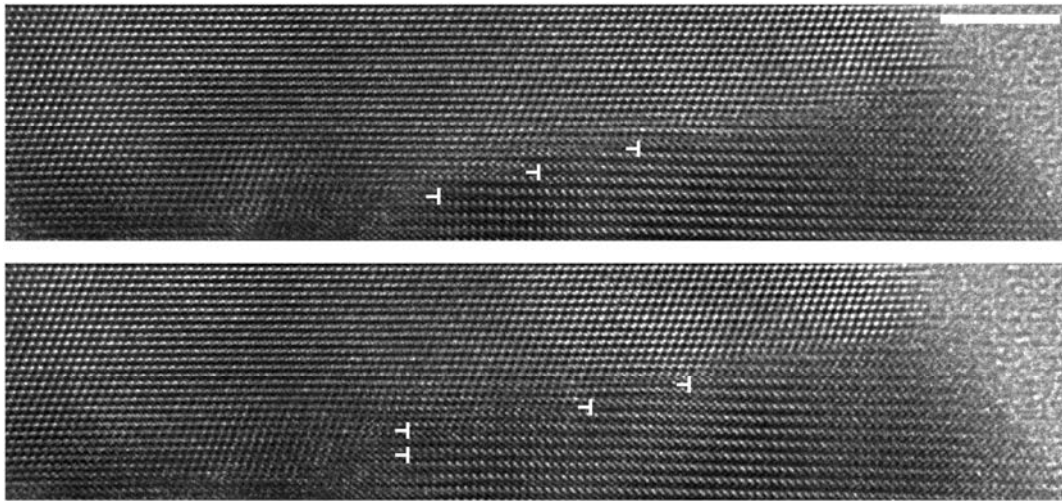


Figure S4. The original TEM images for Figure 3(a) in the main text without labeling of the atomic planes. Scale bar is 5nm.

IV. An estimation of the strain level before and after double-bilayer formation

As discussed in the main text, the nickelide phase nucleated as a train of single-bilayers that experience large elastic stresses due to lattice expansion after nickelide formation. To provide a qualitative analysis of the strain changes before and after the double-bilayer formations, we measured the out-of-plane atomic spacing adjacent to the ledge frontier as a function of time (shown in Figure S5). The details of our measurements are as follows:

- i) We used the 8 HRTEM time-sequences in Figure 2(d) – which is also shown in Figure S3 – for the strain measurements;

ii) Instead of the directly measuring strain in the formed nickelide single-bilayers, we measured the strain level on InGaAs atoms adjacent to the nickelide/InGaAs interface, which are clearer than the nickelide ones. The out-of-plane strain (due to lattice expansion) in the InGaAs side will have the same polarity as in the nickelide side, which is related by the ratio of their moduli.

iii) The strain is measured along InGaAs [111] direction for simplicity, by taking the average of closest 5 atomic distances. The measurement starts from the front of a ledge, and each strain plot corresponds to a ledge labeled by the same color arrow in the HRTEM images in Figure 2(d).

The magnitude and spatial distribution of strain near the InGaAs/nickelide interface at a fixed time frame was plotted in Figure S6 with geometrical phase analysis (GPA) tool¹³ within the DigitalMicrograph(Gatan) package.

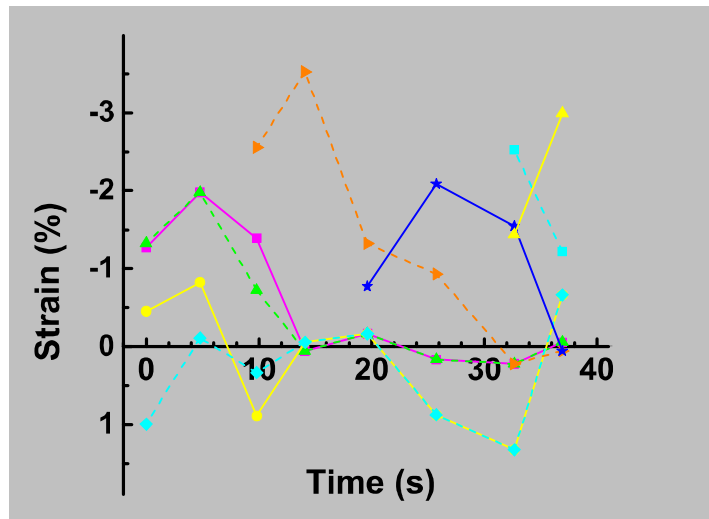


Figure S5. Out-of-plane strain distribution as a function of time. The strain data are color matched to single-bilayer labels in Figure 2d of main text. Generally, a single-bilayer nucleus displayed an initial compressive strain (e.g. green and pink data). This strain generally increased with time as the ledge expanded (e.g. green and pink second data point at 4''46''). When another single-bilayer ledge nucleated (e.g. orange data at 9''49''), the strain energy in a prior formed single-bilayer decreased (e.g. green and pink data at 9''49''). The strain level then gradually decreased due to the generation of misfit dislocation (e.g. green data at 14''05'') and in some cases even changed the polarity to tensile strain (e.g. orange data at 32''39''). After the other single-bilayer reach the front previously formed single-bilayer and formed a double-bilayer ledge, the strain was then close to zero.

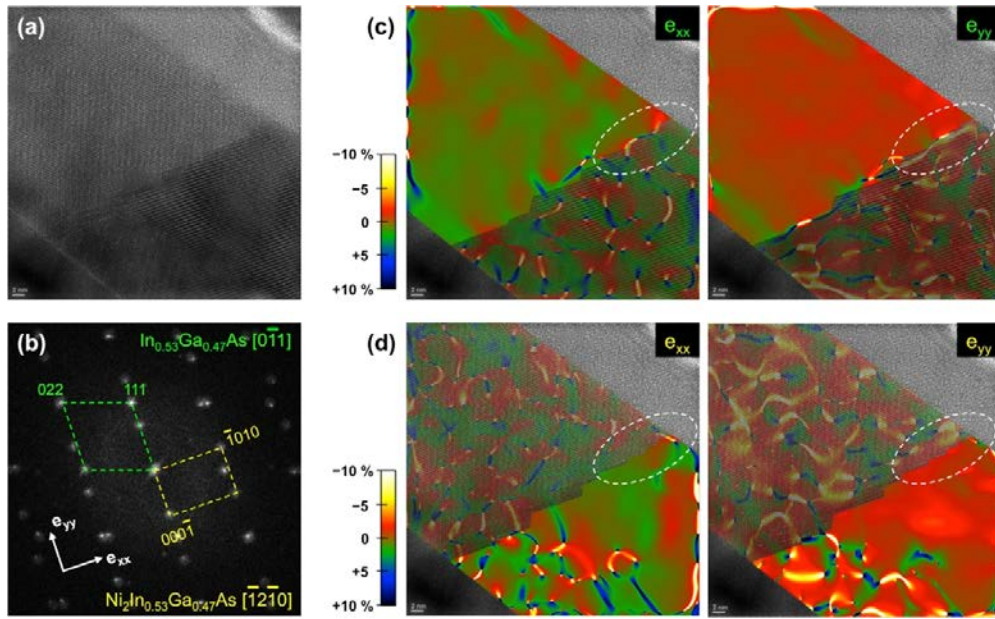


Figure S6. The strain distribution across the interfacial area at a fixed time frame. (a) HRTEM image that is extracted from Movie S1. (b) The FFT image showing the diffraction patterns of $\text{In}_{0.53}\text{Ga}_{0.47}\text{As}$ along the $[0\bar{1}1]$ zone axis and of $\text{Ni}_2\text{In}_{0.53}\text{Ga}_{0.47}\text{As}$ along the $[\bar{1}2\bar{1}0]$ zone axis. The green and yellow boxes enclose diffraction patterns that were used for the GPA map in (c) and (d) respectively. (c) In-plane (e_{xx}) and out-of-plane (e_{yy}) strain distributions for $\text{In}_{0.53}\text{Ga}_{0.47}\text{As}$ side, (d) e_{xx} and e_{yy} distributions for $\text{Ni}_2\text{In}_{0.53}\text{Ga}_{0.47}\text{As}$ side. From both (c) and (d) we observed that the top-right corner of the nickelide/InGaAs interface showed higher strain where the single-bilayer nucleus formed, and that the e_{yy} is stronger than e_{xx} in both nickelide and InGaAs phase near the interface due to volume expansion.

V. Derivation of the nucleation model at nanowire/nickelide interface

Considering a classic nucleus with disc shape on the InGaAs/nickelide interface, heterogeneous and homogeneous nuclei are schematically illustrated in Figure S3.

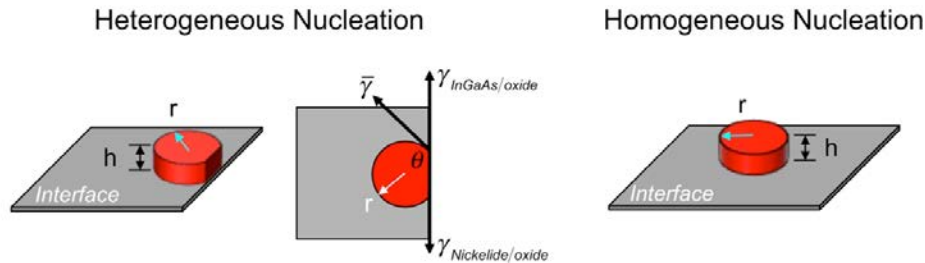


Figure S7. Schematics of heterogeneous and homogeneous nuclei with disc shape with interfacial forces that determine the contact angle θ .

(1) Thermodynamic considerations

In the heterogeneous nucleation situation, the total change in the system free energy is:

$$\Delta G_{hetero} = -\Delta g \cdot V_{disc} + \bar{\gamma} \cdot S_{disc-side} + (\gamma_{nickelide/oxide} - \gamma_{InGaAs/oxide}) \cdot S_{flat-side} + E_{strain} \cdot V_{disc} \quad (S1)$$

where Δg is the nickelide formation energy, $\bar{\gamma}$ is the average InGaAs/nickelide interfacial energy, $\gamma_{nickelide/oxide}$ and $\gamma_{InGaAs/oxide}$ are the interfacial energies of nickelide/oxide and InGaAs/oxide respectively, and E_{strain} is the elastic strain energy for the nickelide nucleus.

Here,

$$V_{disc} = \pi r^2 h \cdot \frac{2\theta}{2\pi} + r^2 \sin(\pi - \theta) \cos(\pi - \theta) h = r^2 h \cdot (\theta - \sin \theta \cos \theta) \quad (S2)$$

$$S_{disc-side} = 2\pi r h \cdot \frac{2\theta}{2\pi} = 2\theta r h \quad (S3)$$

$$S_{flat-side} = 2r h \sin(\pi - \theta) = 2r h \sin \theta \quad (S4)$$

$$\text{We also have the Young's equation of: } \gamma_{nickelide/oxide} - \gamma_{InGaAs/oxide} = \bar{\gamma} \cdot \cos(\pi - \theta) \quad (S5)$$

Therefore,

$$\Delta G_{hetero} = (E_{strain} - \Delta g) \cdot r^2 h \cdot (\theta - \sin \theta \cos \theta) + \bar{\gamma} \cdot 2r h \cdot (\theta - \sin \theta \cos \theta) \quad (S6)$$

As critical nucleus size can be calculated at the peak of the energy barrier,

$$\left. \frac{\partial \Delta G_{hetero}}{\partial r} \right|_{r=r^*} = 0, \text{ and therefore } r^* = \frac{\bar{\gamma}}{\Delta g - E_{strain}}. \quad (S7)$$

By substituting r^* into equation S6, the energy barrier for heterogeneous nucleation can be obtained as,

$$\Delta G_{hetero}^* = \frac{\bar{\gamma}^2 h}{\Delta g - E_{strain}} \cdot (\theta - \sin \theta \cos \theta). \quad (S8)$$

Homogeneous nucleation is equivalent to the case when $\theta = \pi$, for which,

$$\frac{\Delta G_{hetero}^*}{\Delta G_{homo}^*} = \frac{\theta - \sin \theta \cos \theta}{\pi}. \quad (S9)$$

(2) Kinetic considerations

The nucleation rate¹⁴ can be characterized as:

$$R = \omega C \exp\left(-\frac{\Delta G_D}{kT}\right) \exp\left(-\frac{\Delta G^*}{kT}\right) \quad (\text{S10})$$

where ω is the frequency related to atomic vibrations, C is the concentration of critical sized nucleus, ΔG_D is the activation energy for Ni atoms to diffuse to the reaction interface, and ΔG^* is the energy barrier for nucleus.

Therefore,

$$\frac{R_{hetero}}{R_{homo}} = \frac{C_{hetero}}{C_{homo}} \exp\left(\frac{\Delta G_D^{volume} - \Delta G_D^{surface}}{kT}\right) \exp\left(\frac{\Delta G_{homo}^* - \Delta G_{hetero}^*}{kT}\right) \quad (\text{S11})$$

In our previous study,¹² we extracted the value of activation energy for volume diffusion and surface diffusion from Arrhenius plots and obtained:

$$\Delta G_D^{volume} = 1.25 \text{ eV}, \text{ and } \Delta G_D^{surface} = 1.14 \text{ eV}$$

We also know that the surface diffusion is related to the mono-layer atoms at the surface, while the volume diffusion is related to the entire channel cross-section. Therefore,

$$\frac{C_{hetero}}{C_{homo}} \approx \frac{30nm \times 0.588nm}{30nm \times 35nm} = 0.0168. \quad (\text{S12})$$

Also,

$$\frac{R_{hetero}}{R_{homo}} \approx 1.26 \exp\left(\frac{\Delta G_{homo}^* - \Delta G_{hetero}^*}{kT}\right). \quad (\text{S13})$$

VI. The profile of protruded nickelide phase at the reaction-front

In this in-situ study, we observed a slanted (angled) interface at the reaction front, which was the $\text{In}_{0.53}\text{Ga}_{0.47}\text{As} (111) \parallel \text{Ni}_2\text{In}_{0.53}\text{Ga}_{0.47}\text{As} (0001)$ interface. The nickelide phase was always found protruded at the base of $\text{In}_{0.53}\text{Ga}_{0.47}\text{As}$ nanowire (shown in Figure 2(a) and schematically in Figure S4(a)), even though there are two identical $\{111\}$ -type facets of $\text{In}_{0.53}\text{Ga}_{0.47}\text{As}$, i.e. (111) and $(\bar{1}\bar{1}\bar{1})$, that are perpendicular to the $[0\bar{1}1]$ zone axis that $\text{Ni}_2\text{In}_{0.53}\text{Ga}_{0.47}\text{As}$ phase can grow on. This observation was consistent in all (more than 10) in-situ specimens that we prepared.

To understand this behavior, we did multiple tests with various sample conditions, and finally realized that the direction of the protruded interface at reaction-front was controlled by the interfacial condition between initially deposited HfO_2 layer and the $\text{In}_{0.53}\text{Ga}_{0.47}\text{As}$ nanowire channel. As shown in Figure S4, the HfO_2 layers were initially deposited on $\text{In}_{0.53}\text{Ga}_{0.47}\text{As}$ by atomic layer deposition (ALD) with two different pretreatment: (type I) 5 consecutive cycles of tetramethylammonium (TMA) pulse and H_2 plasma, and (type II) only 5 pulses of H_2 plasma. In all our samples, $\text{In}_{0.53}\text{Ga}_{0.47}\text{As}$ native oxide was stripped by diluted HCl dip before immediate loading into the ALD chamber. We observed that the slanted $\text{In}_{0.53}\text{Ga}_{0.47}\text{As}$ /nickelide reaction-front protruded at base of the nanowire channel (i.e. $\text{In}_{0.53}\text{Ga}_{0.47}\text{As}/\text{HfO}_2$ interface) in type I specimen, while the reaction-front protruded at top of the nanowire channel (i.e. $\text{In}_{0.53}\text{Ga}_{0.47}\text{As}/\text{SiO}_2$ interface) in type II specimen. It was reported that H_2 plasma pretreatment could effectively remove the native oxide and decap the As-As dimers at InGaAs surface,¹⁵ together with the self-cleaning property of ALD- HfO_2 ,¹⁶ resulting in an oxide-free InGaAs/ HfO_2 interface with the dominant interfacial bond by Ga-O bonds (formed between Ga-terminated InGaAs surface and O-terminated HfO_2 surface).¹⁷ Moreover, the consecutive TMA pulse and H_2 plasma pretreatment not only can remove the native oxide at InGaAs surface, but also can passivate the As-As dimers by forming As-Al-As bridge bonds,¹⁸ resulting in an Al-terminated interface and replacing part or all of the Ga-O bonds to Al-O bonds.¹⁹

Therefore, our conclusion is that interfacial conditions in between $\text{In}_{0.53}\text{Ga}_{0.47}\text{As}/\text{HfO}_2$, either it's Ga-O bonds or Al-O bonds, can flip the protruded profiles at $\text{In}_{0.53}\text{Ga}_{0.47}\text{As}$ /nickelide reaction-front, even though the nickelide phase always nucleated at the top surface of nanowire channel (from both experimental observations and our model analysis).

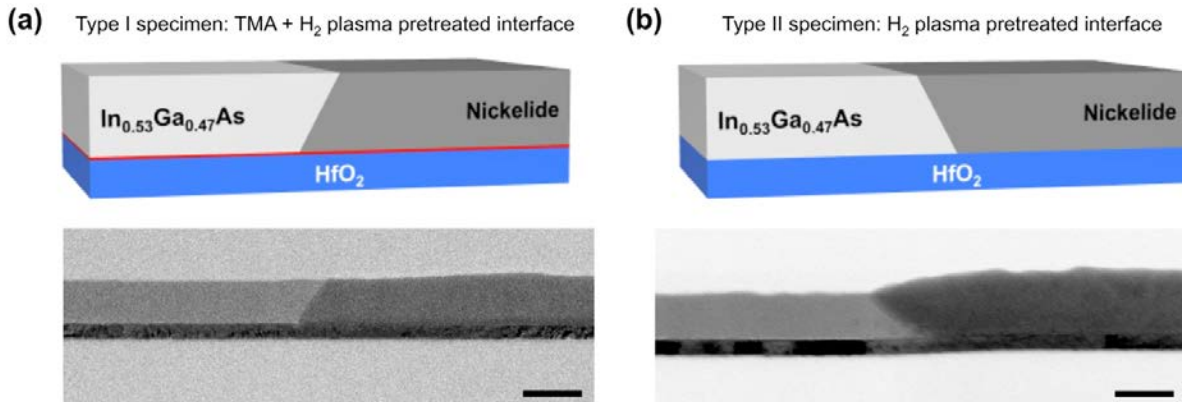


Figure S8. Comparison of the interfacial profiles at nickelide reaction-front that were controlled by different $\text{In}_{0.53}\text{Ga}_{0.47}\text{As}/\text{HfO}_2$ interfacial conditions. (a) Schematic and TEM image of the type I specimen. In this type of sample, HfO_2 layer was initially deposited on $\text{In}_{0.53}\text{Ga}_{0.47}\text{As}$ by ALD with pretreatment of 5 consecutive cycles of TMA pulse and H_2 plasma. The interface was dominated by Al-O bonds. After nickelide reaction,

the nickelide phase was protruded at the base of nanowire. (b) Schematic and TEM image of the type II specimen. In this type of sample, HfO₂ layer was initially deposited on In_{0.53}Ga_{0.47}As by ALD with pretreatment of only 5 pulses of H₂ plasma only. The interface was dominated by Ga-O bonds. After nickelide reaction, the nickelide phase was protruded at the top of nanowire. Scale bars are 50 μm.

References

- 1 Egerton, R., Li, P. & Malac, M. Radiation damage in the TEM and SEM. *Micron* **35**, 399-409 (2004).
- 2 Taheri, M. L. *et al.* Current status and future directions for in situ transmission electron microscopy. *Ultramicroscopy* **170**, 86-95 (2016).
- 3 Lian, J., Wang, L., Sun, K. & Ewing, R. C. In situ TEM of radiation effects in complex ceramics. *Microscopy research and technique* **72**, 165-181 (2009).
- 4 Carter, C. B. & Williams, D. B. *Transmission electron microscopy*. (Springer-Verlag US, 2016).
- 5 De Jonge, N. & Ross, F. M. Electron microscopy of specimens in liquid. *Nature nanotechnology* **6**, 695-704 (2011).
- 6 Liang, W.-I. *et al.* In Situ Study of Fe₃Pt-Fe₂O₃ Core-Shell Nanoparticle Formation. *Journal of the American Chemical Society* **137**, 14850-14853 (2015).
- 7 Liang, W.-I. *et al.* In Situ Study of Spinel Ferrite Nanocrystal Growth Using Liquid Cell Transmission Electron Microscopy. *Chemistry of Materials* **27**, 8146-8152 (2015).
- 8 Liu, X. H. *et al.* In situ atomic-scale imaging of electrochemical lithiation in silicon. *Nature nanotechnology* **7**, 749-756 (2012).
- 9 Tang, W. *et al.* Nucleation and Atomic Layer Reaction in Nickel Silicide for Defect-Engineered Si Nanochannels. *Nano Letters* **13**, 2748-2753 (2013).
- 10 Czornomaz, L. *et al.* CMOS compatible self-aligned S/D regions for implant-free InGaAs MOSFETs. *Solid-State Electronics* **74**, 71-76 (2012).
- 11 Han, L. *et al.* Interrogation of bimetallic particle oxidation in three dimensions at the nanoscale. *Nature Communications* **7** (2016).
- 12 Chen, R. & Dayeh, S. A. Size and Orientation Effects on the Kinetics and Structure of Nickelide Contacts to InGaAs Fin Structures. *Nano letters* **15**, 3770-3779 (2015).
- 13 Hÿtch, M. J., Snoeck, E. & Kilaas, R. Quantitative measurement of displacement and strain fields from HREM micrographs. *Ultramicroscopy* **74**, 131-146 (1998).
- 14 Porter, D. A., Easterling, K. E. & Sherif, M. *Phase Transformations in Metals and Alloys, (Revised Reprint)*. (CRC press, 2009).
- 15 Kim, E. J. *et al.* Atomically abrupt and unpinned Al₂O₃/In_{0.53}Ga_{0.47}As interfaces: Experiment and simulation. *Journal of Applied Physics* **106**, 124508 (2009).

- 16 Hinkle, C. *et al.* GaAs interfacial self-cleaning by atomic layer deposition. *Applied Physics Letters* **92**, 071901 (2008).
- 17 Wang, W., Xiong, K., Wallace, R. M. & Cho, K. Impact of interfacial oxygen content on bonding, stability, band offsets, and interface states of GaAs: HfO₂ interfaces. *The Journal of Physical Chemistry C* **114**, 22610-22618 (2010).
- 18 Melitz, W., Shen, J., Kent, T., Kummel, A. C. & Droopad, R. InGaAs surface preparation for atomic layer deposition by hydrogen cleaning and improvement with high temperature anneal. *Journal of Applied Physics* **110**, 013713 (2011).
- 19 Cai, G., Sun, Q., Jia, Y. & Liang, E. Al passivation effect at the HfO₂/GaAs interface: A first-principles study. *Materials Science in Semiconductor Processing* **41**, 1-5 (2016).